

POLITECNICO DI TORINO

Corso di laurea magistrale in ingegneria energetica
e nucleare



Master of science thesis

Development of a model for the dynamic performance characterization of a scroll expander

Supervisors:

Prof. Daniela Misul

Prof. Mirko Baratta

Candidate:

Andrea Neirotti

July 2020

Ringraziamenti

Vorrei innanzitutto ringraziare il professor Baratta e la professoressa Misul per avermi permesso di svolgere questa tesi e per l'aiuto che mi hanno fornito.

Inoltre, voglio esprimere la mia riconoscenza a Riccardo e all'ingegner Nespoli per l'importante supporto che ho ricevuto durante la stesura della tesi.

Un grazie infinito va alla mia famiglia che mi ha sempre assecondato e mi ha permesso di studiare in piena serenità.

Infine, un grazie di cuore va alla mia dolce Veronica. Sei la mia forza.

Contents

Chapter 1	1
Chapter 2	6
2.1 Involute of a circle.....	6
2.2 Scroll geometry	7
2.3 Rotation of the orbiting scroll	9
2.4 Modification of the scroll profile.....	11
2.5 Volumes of the chambers	12
2.6 Built-in volume ratio and pressure ratio	14
Chapter 3	15
3.1 Choked flow	15
3.1.1 Inlet flow.....	16
3.1.2 Outlet flow	18
3.2 Internal leakage area and leakage flow.....	19
3.2.1 Radial leakage	20
3.2.2 Flank leakage	22
3.3 Second law of dynamics.....	22
3.4 The principle of mass conservation	25
3.5 First principle of thermodynamic.....	26
3.6 DC generator.....	31
Chapter 4	32
4.1 Over\unders expansion	35
4.2 Scroll expander losses	36
4.3 DC generator losses	37
Chapter 5	39
5.1 Scrolls tips modification and gaskets	39
5.2 The geometric data	41
5.3 Properties of materials and of air	42

5.4	Leakage flow data	43
5.5	DC generator.....	44
Chapter 6	45
6.1	Angular speed and orbital angle	46
6.2	Chambers volumes.....	47
6.3	Chambers pressures.....	48
6.4	Chambers temperature.....	50
6.5	Inlet and outlet mass flow rates.....	53
6.6	Power and Efficiencies	54
Chapter 7	57
7.1	Inlet pressure variation	57
7.2	Axial and radial clearance variation	61
Chapter 8	67
Nomenclature	68
Bibliography	71

Abstract

The aim of this thesis is to present a model for studying the dynamic behaviour of scroll expanders. The latter are volumetric machines that generate mechanical power expanding high pressure gas/vapor in two or more variable volume chambers. The first step consists in the description of the device geometry, the final purpose is the calculation of the expansion chambers volume. In this section, starting from the involute of the circle, are introduced all the quantities needed for the subsequent development of the model. After that the thermodynamic model is presented. It allows to calculate the pressures and temperatures inside each chamber. In addition, the equations used to calculate the working fluid losses, the heat exchanged and the torque are explained. Then is introduced the concept of efficiency that is useful to compare the device in different operating conditions. In the last part of this thesis are shown the results of the simulation with brief comments. Finally, is performed a sensitivity analysis about the inlet pressure and radial and axial clearances.

Chapter 1

Introduction

In the coming years the energetic sector will face the issue of the emission produced by the use of fossil fuels. To understand how urgent this theme is in Figure 1.1 are shown the world total primary energy consumption by source and the shares of primary energy from 1970 to 2040. It is clear that most of the energy that will be used in the next years will continue to be provided by fossil fuels. This is a dangerous trend because many scientific researches have demonstrated the correlation between the number of extreme climatic events and the quantity of greenhouse gases (GHG) in atmosphere. Besides, most of the time, these extreme climatic events affect the least resilient nations producing a lot of economic, social and ambient damages. If in the next years there will be not a reduction of the GHG emission, the extreme natural phenomena will increase in number and in harmfulness.

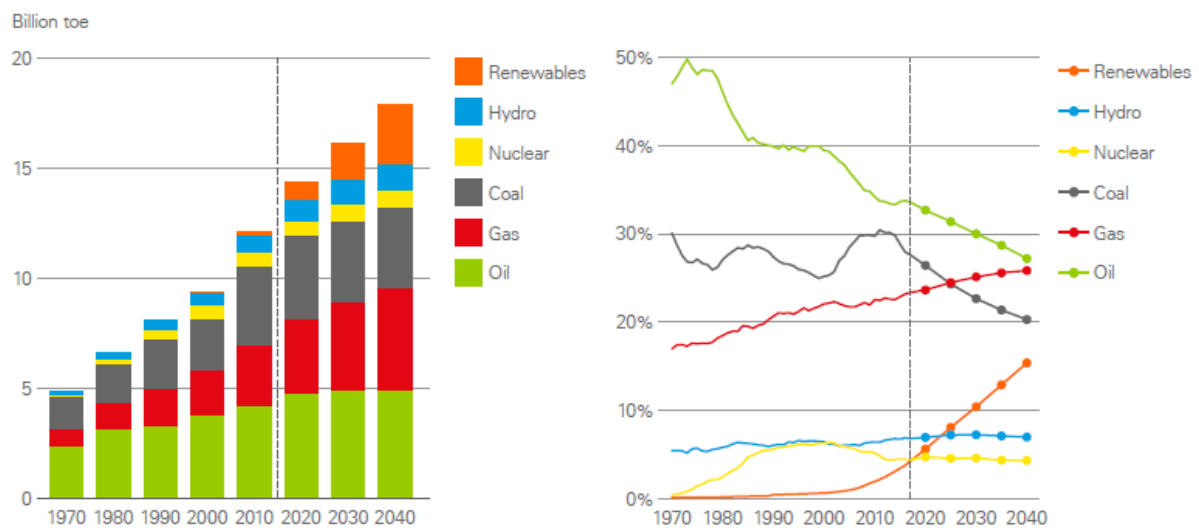


FIGURE 1.1 PRIMARY ENERGY CONSUMPTION BY FUEL AND SHARES OF PRIMARY ENERGY [1]

Another significant issue linked to the use of fossil fuels is the decreasing EROI (Energy Return On Investment) of the latter. The EROI is the ratio between the energy returned by a fuel and the energy invested to produce it hence, the EROI, represents the accessibility of a resource. The higher is the EROI, the greater is the amount of net energy delivered to society. In Figure 1.2 are shown the oil and gas EROIs of different nations, It is possible to see the downward trend over the years.

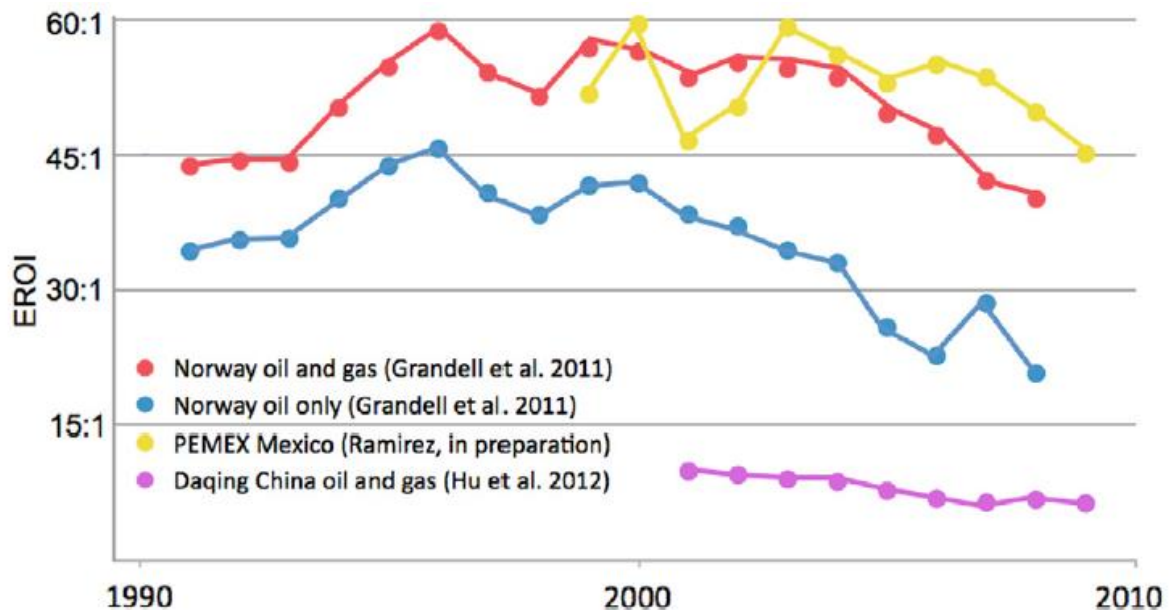


FIGURE 1.2 OIL AND GAS EROI OF VARIOUS COUNTRIES [2]

In the future the solution will be the use of renewable energy sources (RES) of different type to generate all the power required by the human population. The present represents a transition time in which we have the presence of both fossil and renewable energy sources. In this context, when we deal with fossil fuel, is fundamental to increase as much as possible the ratio between the useful energy produced and the emission of GHGs.

Many times, in human activities, is available low-grade heat. Some common examples are the industrial waste heat, the geothermal resources at low enthalpy or the exhaust gases after the combustion of the biomass. In these situations, the plants using organic Rankine cycle (ORC), are an efficient and cost-effective technology to produce electrical-mechanical power from low/medium temperature sources that otherwise would not be technically and economically recoverable with conventional energy systems. Nowadays the cumulative installed capacity of ORC plants is 2.7 GW mainly in geothermal and biomass applications [3]. In Table 1.1 are classified the ORC plants according to heat source temperature and power capacity range.

Regarding the ORC plants one of the most critical component is the expander. The latter can be divided into two categories: the volume-based expanders and the velocity-based expanders. The second comprise radial and axial turbines. The use of axial turbines is confined to those cases in which the order of the power generated is of few MW. Looking at Figure 1.4 is clear that the design and the construction of axial turbines for low powers is not economically convenient. Besides, as shown in Figure 1.3, the efficiency achievable at low powers is not

competitive. Regarding the radial turbines they can be utilized in a wide range of powers, from few to hundreds kW.

TABLE 1.1 [4]

Classification	Heat source temperature [°C]	Classification	Power capacity [kW]
Low	<150	Micro	<3
Medium	150-250	Mini	3-50
High	>250	Small	50-500
		Medium	500-5000
		Large	>5000

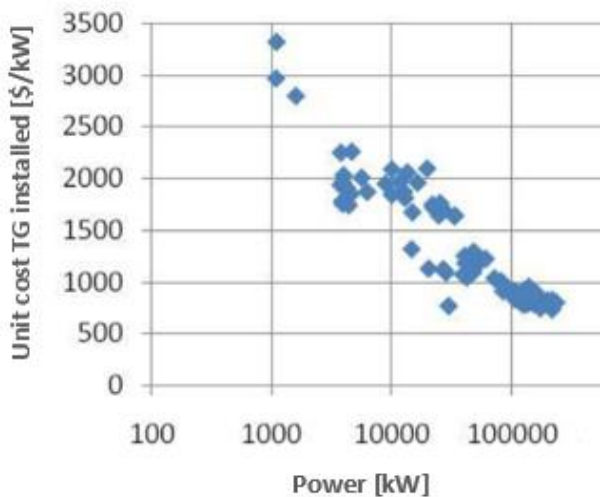


FIGURE 1.4 UNIT COST FOR kW INSTALLED

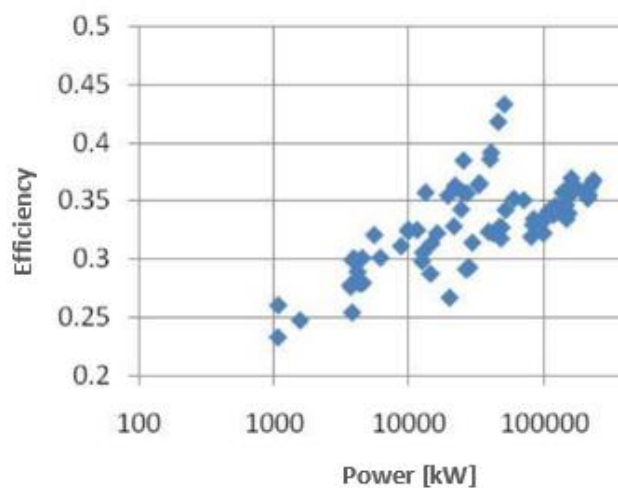


FIGURE 1.3 EFFICIENCY FOR kW INSTALLED

Most of the time in micro or mini ORC installations are exploited the volume-based expanders. They include primarily scroll, screw, piston and roots expanders (they are depicted in Figure 1.5). These machines have a low flow rate even at high pressure ratios and can manage two-phase flows. Among the various types of volumetric expanders, the scroll expanders, seem to be the most promising. Compared to competitors, scroll expanders, may have positive characteristics such as high efficiency, low level of noise and vibration and few moving parts. Moreover, they can be built easily and at low cost and manifest high reliability. Among the disadvantages is possible to list the little power provided, the need of lubrication and the low-pressure ratio which limits their use. In Table 1.2 are collected the values present in the scientific literature for the four expanders.

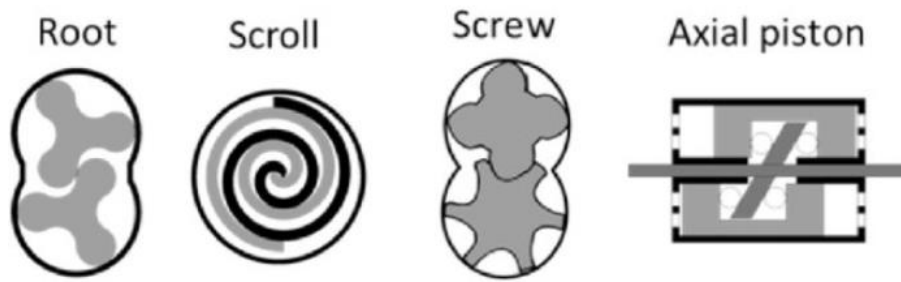


FIGURE 1.5 ROOT, SCROLL, SCREW AND AXIAL EXPANDERS [5]

TABLE 1.2 [5]

Parameter	Scroll	Piston	Screw	Roots
Displacement [l/s]	0.76 ÷ 32	1.25 ÷ 75	25 ÷ 1100	-
Maximum power [kW]	10	10	200	30
Maximum rotational speed [rpm]	10000	3000	21000	20000
Built-in volume ratio	1.5 ÷ 4.2	2 ÷ 14	1 ÷ 8	~ 1
Maximum pressure [bar]	40	70	-	-
Maximum temperature [°C]	250	560	-	-
Two-phase flow handling	yes	low	yes	yes
Isentropic efficiency [%]	87	70	84	47

It is important to say that scroll compressors are already widely used in inverse cycles for heating, ventilation and air conditioning applications. Instead, the sector of scroll expanders, is still in its early stages. Few companies have ventured into the construction of these machines. One of these is Air Squared. In Table 1.3 are shown the two scroll expanders in their catalog. The difficulty to find commercial scroll expanders has induced the researchers to operate scroll compressors as expanders. This is possible because the scroll machines are reversible because there are few differences between scroll expanders and compressors. The pioneer in this field was Yanagisawa et al. [6] who in 1988 utilized an automotive air conditioning scroll compressor as an expander reaching up an adiabatic efficiency between 60 and 75% with a rotational speed in the range 1000÷4000 rpm.

In scientific literature there are three approaches to model the scroll expanders. The first one is based on the thermodynamic methodology, the second is a semi-empirical method and the third consists of CFD (Computational Fluid Dynamic) simulation. In this thesis is presented a detailed and generic model which belongs to the first group. Starting from the geometry description of the device are introduced the equations to calculate the volume of the expansion chambers. The temperatures and the pressures are gotten from the basic principles of physics: the principles of mass and energy conservation and the dynamic laws. Finally, is presented the DC generator model necessary to simulate the electro-mechanical conversion of the power. The final objective of this thesis is to calculate the efficiency of a scroll expander knowing its operational conditions.

TABLE 1.3 [7]

E15H022A-SH



E22H038B-L-SH



Nominal output [kW_e]	1	5
Volume ratio	3.5	3.25
Displacement [cm^3/rev]	14.5	73
Maximum speed [rpm]	3600	2600
Maximum inlet pressure [bara]	13.8	13.8
Maximum inlet temperature [$^{\circ}\text{C}$]	175	175
Nominal sound level [dB(A)]	55	55
Net weight [kg]	9	82

Chapter 2

Description of the scroll expander geometry

The first step to build the dynamic model of a scroll expander is the definition of the main geometric characteristics. The final goal is to define the volume of the expansion chambers as a function of the orbital angle. The geometric quantities that can be directly calculated once the expander has been dismantled are the thickness, the pitch, the number of chambers and the height of the scrolls. From these quantities it is possible to construct the geometric model. All the equations in this chapter are demonstrated in the source [8].

2.1 Involute of a circle

Figure 2.1 shows the involute of a circle which is the most commonly used scroll spiral. The coordinates of involute points are expressed by the following equations:

$$(2.1) \quad x = a(\cos\varphi + \varphi \sin\varphi)$$

$$(2.2) \quad y = a(\sin\varphi - \varphi \cos\varphi)$$

Where:

- a is the basic circle radius,
- φ is the involute angle (corresponding to point M in the Figure 2.1).

Other useful geometric quantities are the radius of the involute ρ , the differential length of the involute dl and the differential area dS . The latter can be calculated using the following equations:

$$(2.3) \quad \rho = \sqrt{x^2 + y^2 - a^2} = \sqrt{a^2(1 + \varphi^2) - a^2} = a\varphi$$

$$(2.4) \quad dl = \rho d\varphi = a\varphi d\varphi$$

$$(2.5) \quad dS = \frac{1}{2}(a\varphi)^2 d\varphi.$$

Integrating dl and dA from 0 to φ is possible to obtain the involute length from point N to point M and the area S between involute and basic circle.

$$(2.6) \quad l = \int_0^\varphi a\varphi d\varphi = \frac{1}{2} a\varphi^2$$

$$(2.7) \quad S = \int_0^\varphi \frac{1}{2} (a\varphi)^2 d\varphi = \frac{1}{6} a^2 \varphi^3.$$

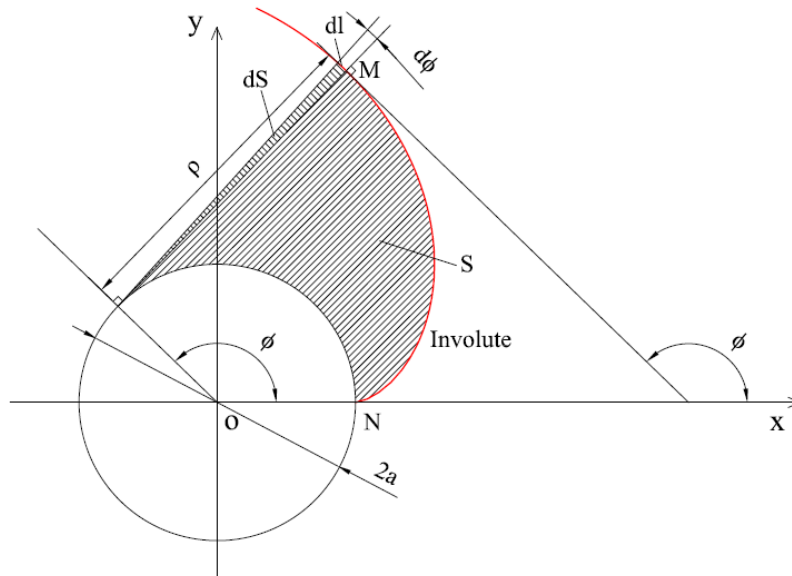


FIGURE 2.1 INVOLUTE OF A CIRCLE [8]

2.2 Scroll geometry

The scroll expander is made up of two identical spirals. One is stationary and is called fixed scroll while the other is named orbiting scroll and is placed by rotating the fixed scroll by 180°. The inner and outer edges of both scrolls are the involute of the basic circle with involute angles of α and $-\alpha$ respectively. The coordinates of these two involutes are obtained by the following equations:

$$(2.8) \quad x_i = a(\cos\varphi_i + (\varphi_i - \alpha)\sin\varphi_i)$$

$$(2.9) \quad y_i = a(\sin\varphi_i - (\varphi_i - \alpha)\cos\varphi_i)$$

$$(2.10) \quad x_o = a(\cos\varphi_o + (\varphi_o + \alpha)\sin\varphi_o)$$

$$(2.11) \quad y_o = a(\sin\varphi_o - (\varphi_o + \alpha)\cos\varphi_o).$$

Calculating the abscissa and the ordinate of the points A, B and C in Figure 2.2 is possible to get the pitch and the thickness of the scroll. Below the equations for the general case:

$$(2.12) \quad t_s = 2a\alpha$$

$$(2.13) \quad Pit = 2\pi a.$$

It is also possible to compute the orbiting radius R_{orb} (see the next paragraph), the end involute angle φ_e and the radius of the shell R_{sh} . For the general case are obtained the following equations:

$$(2.14) \quad R_{orb} = \pi a - 2a\alpha$$

$$(2.15) \quad \varphi_e = \left(2N_c + \frac{1}{2}\right)\pi$$

$$(2.16) \quad R_{sh} = \sqrt{(a(\varphi_e + \alpha) + R_{orb})^2 + a^2}$$

Where N_c is the number of expansion chambers.

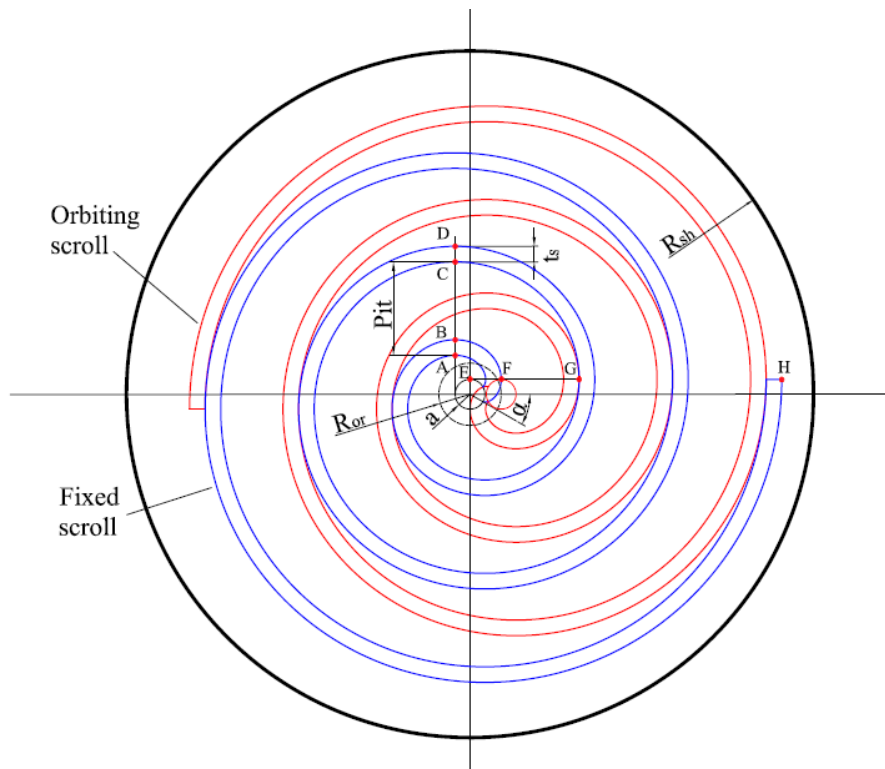


FIGURE 2.2 MAIN SCROLL PARAMETERS [8]

2.3 Rotation of the orbiting scroll

During the expansion the orbiting scroll moves anticlockwise along a circular orbit with radius equal to R_{orb} . It is fundamental to understand that the orbiting scroll does not rotate on itself but orbits around the centre of the fixed scroll. In other words, all the points which constitute the orbiting scroll have a circular trajectory with different centres. The high-pressure working fluid enters from the suction port at the centre and expands generating the orbiting motion. The mechanical power is delivered through an eccentric shaft. Looking at the Figure 2.3 it is clear that the rotation must be anti-clockwise otherwise the effect produced is to compress the fluid as happens inside a scroll compressor.

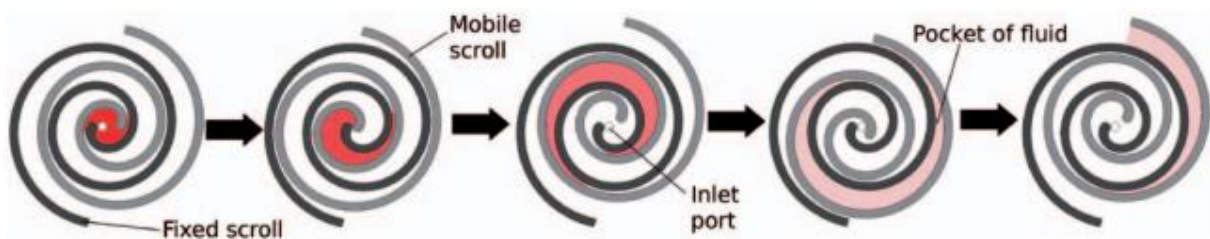


FIGURE 2.3 WORKING PRINCIPLE OF A SCROLL EXPANDER [9]

The Figure 2.4 shows in more detail the rotation of the orbiting scroll. The orbiting angle ϑ is the angle included between the horizontal axis and the line passing through the centres of the two basic circles. It ranges from 0 to 2π . The expander depicted is constituted of 4 expansion chambers plus the discharge one. In the figure each chamber is represented with its number. DC means "discharge chamber" while the notation 1-2 indicates that the first two rooms are joined (see the next paragraph). In the centre of the figure is present the legend that will be valid for all the paper. When the orbital angle is equal to zero all the expansion chambers are at their maximum volume while the discharge chamber is at its minimum. With an infinitesimal increase of the orbital angle all the volumes of the expansion chambers restart from their minimum whilst the volume of the discharge chamber resumes from its maximum. During the rotation all the expansion chambers volumes increase while that of the discharge room reduces because the volume of the shell is constant. This sequence is repeated continuously. When the orbital angle passes from 2π to $0+d\vartheta$ the i -th room becomes the $(i+1)$ th. This means that the volume grows without discontinuities. The mesh points as those points in which the inner or outer involute of the orbiting scroll touch respectively the outer or inner involute of the fixed scroll.

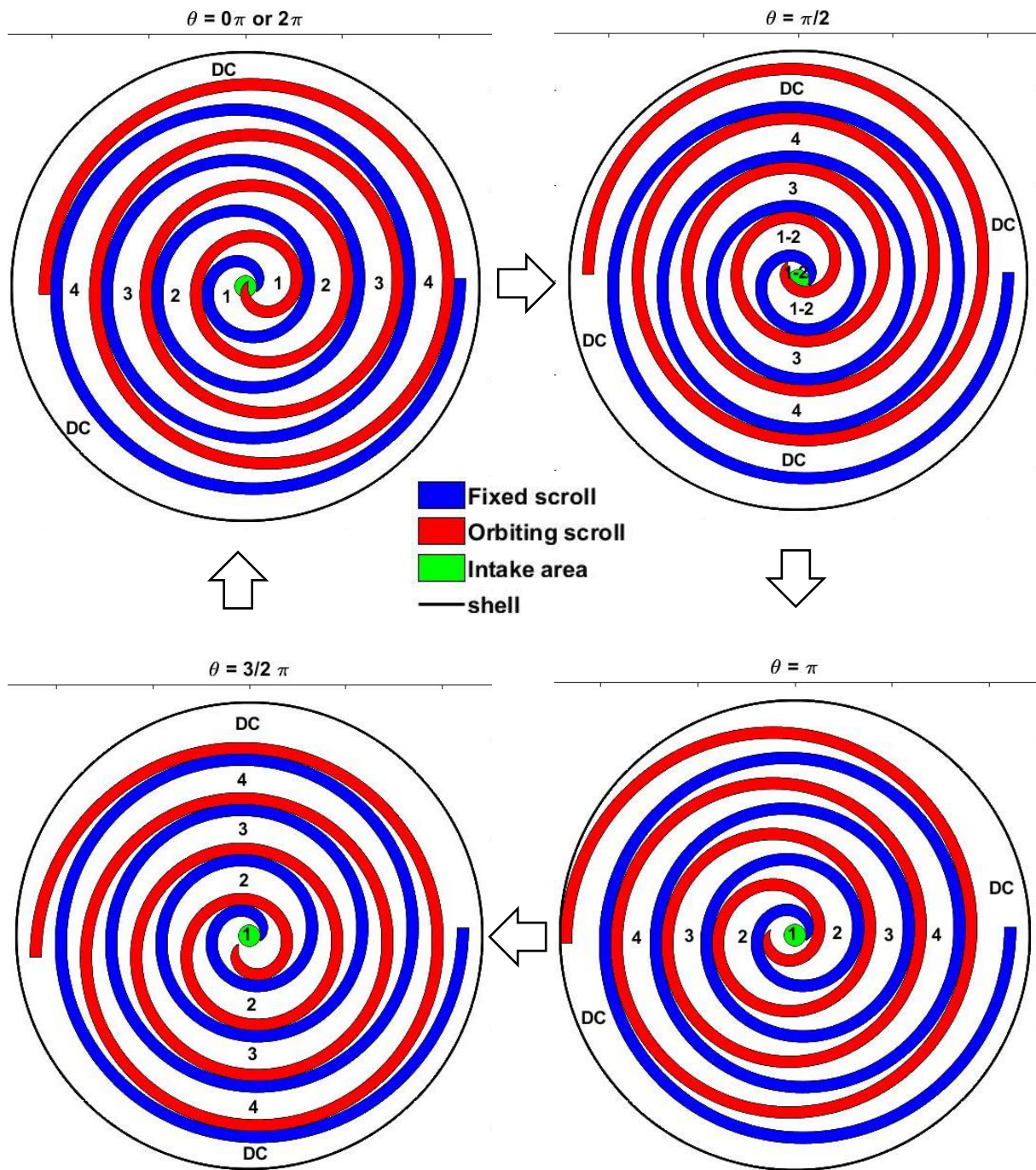


FIGURE 2.4 POSITION OF THE ORBITING SPIRAL AT DIFFERENT ORBITAL ANGLE

2.4 Modification of the scroll profile

The scroll tip geometry needs to be modified to achieve high efficiency, light weight and easy manufacture. The three most common ways to modify the spirals in the suction area are shown in Figure 2.5. Specifically they are the single arc, dual arc and perfect mesh profile (PMP) design.

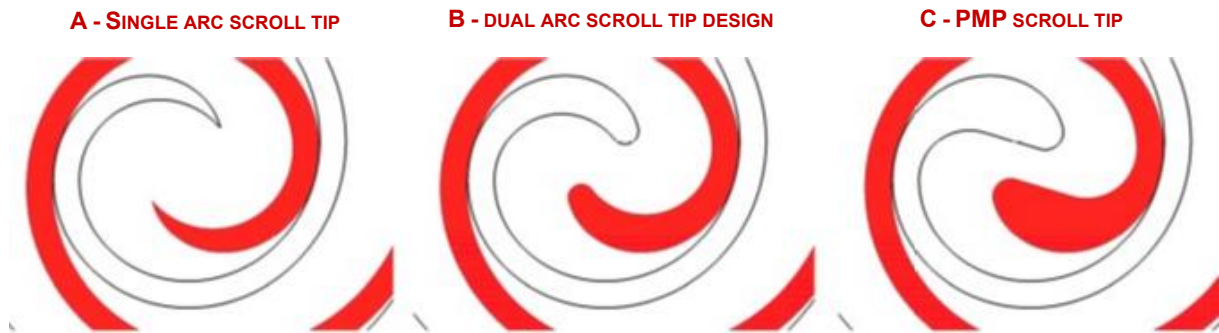


FIGURE 2.5 SCROLL TIP DESIGN VARIATIONS [10]

The device that has been analysed in this thesis presents the first type of scroll tip design that can be obtained by a circular cutting. The geometry of the scroll tip has an impact on the inlet mass flowrate since during the expansion part of the suction port is covered by the tip of the orbiting scroll. In Figure 2.6 the area highlighted in yellow is removed by the circular cutting. The final shape of the scroll is represented by the blue line. The cutter circle centre is located in the intersection point between the basic circle and the left side of the x axis.

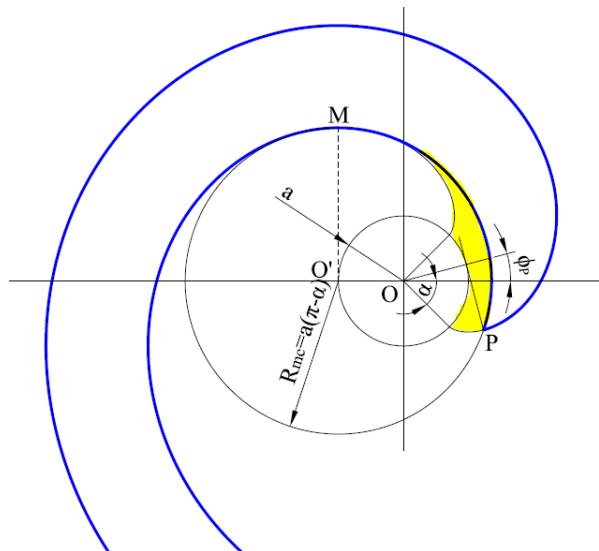


FIGURE 2.6 GEOMETRY OF THE SINGLE ARC SCROLL TIP [8]

The radius of the cutter can be calculated with the formula:

$$(2.17) R_{mc} = a(\pi - \alpha).$$

The point P in the sharp corner has an involute angle that can be found solving numerically the following equation:

$$(2.18) (\varphi_p + \alpha)^2 + 2\cos\varphi_p + 2\cos(\varphi_p + \alpha)\sin\varphi_p = (\pi - \alpha)^2 - 2.$$

With this modification, at the beginning of the rotation, the first expansion chamber is connected to the second since the part of the wall that separated the two rooms is missing. The two chambers separate when point P becomes the mesh point. The disconnection orbiting angle can be calculated with the expression:

$$(2.19) \vartheta_{disc} = \varphi_p + \frac{\pi}{2}.$$

In Figure 2.7 are displayed the first two chambers before and after the disconnection. In the first case there is only one chamber that will be called “merged chamber” or “chamber 1-2”. In the second one there are two distinct chambers: “chamber 1” and “chamber 2”.

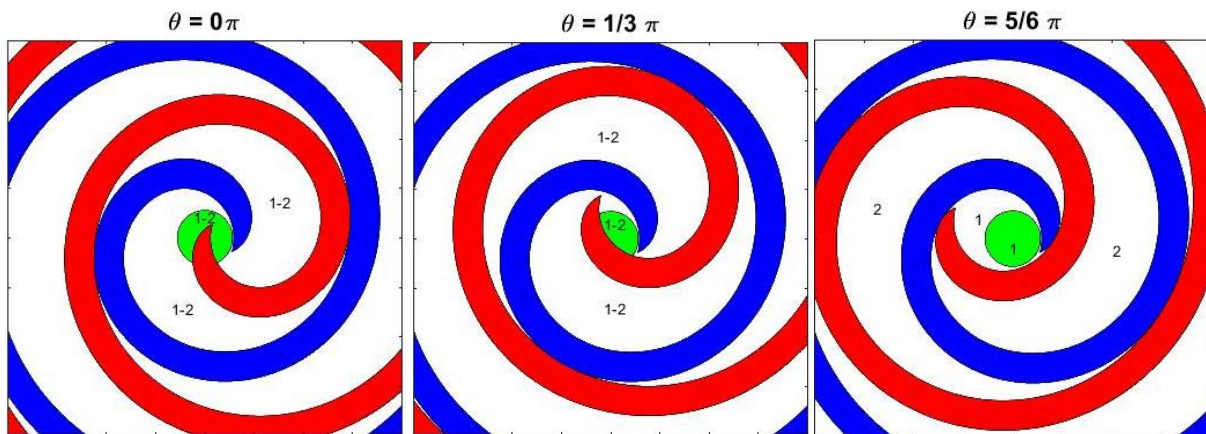


FIGURE 2.7 FRIST AND SECOND CHAMBER BEFORE AND AFTER THE DISCONNECTION

2.5 Volumes of the chambers

In this paragraph have been collected the equations to calculate the volume of the chambers. All the expansion chambers are confined between the inner involute of one spiral and the outer involute of the other spiral. It is important to note that every expansion chamber is composed by two parts. In Figure 2.8 they have been called “right” and “left” (for simplicity has been considered an expander with two expansion chambers).

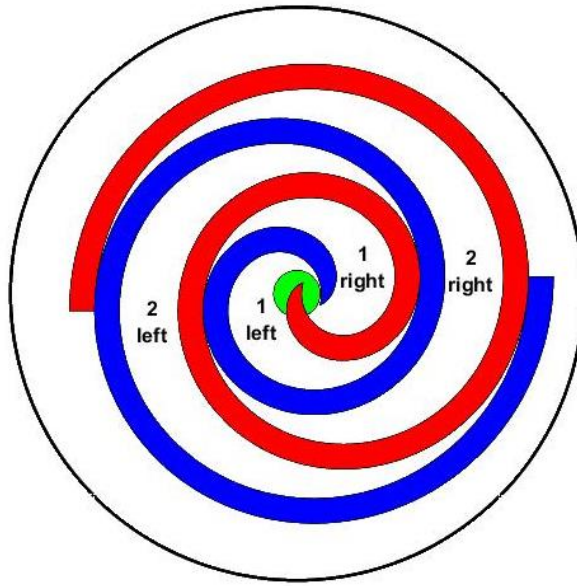


FIGURE 2.8 DIVISION OF THE EXPANSION CHAMBERS

The volume of the i -th chamber is calculated with:

$$(2.20) \quad V_{Ci} = 4\pi a^2 h_s (\pi - 2\alpha) (\vartheta - 3\pi + 2i\pi)$$

Where:

- h_s is the height of the scroll
- i represents the chamber considered with $2 \leq i \leq N_C$.

As far as the volume of the first chamber is concerned ($i = 1$) it can be calculated with the following equation:

$$(2.21) \quad V_{C1} = h_s \left\{ \frac{a^2}{3} \left[\left(\frac{\pi}{2} + \vartheta - \alpha \right)^3 - \left(-\frac{\pi}{2} + \vartheta + \alpha \right)^3 \right] - a^2 (\pi - 4\alpha) \right\} + V_{mc}$$

Where:

$$(2.26) \quad V_{mc} = 2h_s \left[a^2 \left(\frac{\alpha^2 + \varphi_p^2 + 2\alpha\varphi_p - 1}{4} \sin(2\varphi_p) + \frac{\alpha + \varphi_p}{2} \cos(2\varphi_p) - \frac{\sin(2\alpha)}{4} + \frac{(\alpha + \varphi_p)^3}{6} \right) + \frac{\pi a^2 (\pi - \alpha)^2}{4} - \frac{\pi a^2}{2} - \frac{a^2 (\pi - \alpha)^3}{6} - \frac{\alpha a^2}{2} + \frac{a^2 \sin\alpha \cos\alpha}{2} + \frac{\gamma R_{mc}^2}{2} - \frac{R_{mc}^2 \sin\gamma \cos\gamma}{2} \right]$$

$$(2.27) \quad R_{mc} = a(\pi - \alpha)$$

$$(2.28) \quad \gamma = \sin^{-1} \frac{|a(\sin\varphi_p - (\varphi_p + \alpha)\cos\varphi_p)|}{R_{mc}}$$

The term V_{mc} is the volume removed from the spirals by the circular cutting. It corresponds to the volume of the yellow part in Figure 2.6. It is remarkable to remember that before the disconnection ($\vartheta \leq \vartheta_{disc}$) the first and the second expansion room are connected and so the volume of the chamber 1-2 is the sum of the volumes of the first two chambers ($V_{C1-2} = V_{C1} + V_{C2}$). Instead, after the disconnection ($\vartheta > \vartheta_{disc}$), the two volumes are separated and calculated with equation 2.20 and 2.21. Lastly the discharge chamber volume ($i = N_c + 1$) is obtained subtracting from the volume of the shell that of all the expansion rooms plus that of the two spirals.

$$(2.22) \quad V_{dis} = \pi h_s R_{sh}^2 - \sum_{i=1}^{i=N_c} V_{Ci} - 2h_s S_s$$

Where $S_s = a^2 \alpha \left(\varphi_e^2 + \frac{\alpha^2}{3} \right)$.

2.6 Built-in volume ratio and pressure ratio

The built-in volume ratio, r_v , is defined as the ratio between the discharge chamber volume at the beginning of the discharge process and the maximum suction chamber volume [11]:

$$(2.29) \quad r_v = \frac{V_{dis,max}}{V_{suc,max}}$$

So, once the main geometrical quantities are defined, the built-in volume ratio is constant.

The pressure ratio is defined as the ratio between the suction pressure and the discharge pressure [11]:

$$(2.30) \quad r_p = \frac{P_{suction}}{P_{discharge}}$$

The efficiency of scroll expanders depend heavily on pressure ratio and built-in volume ratio.

Chapter 3

Thermodynamic model

After the geometric model presentation is necessary to introduce the equations that rule the expansion. The principle of mass conservation and the first law of thermodynamics allow to evaluate the pressure and the temperature inside the rooms while the volume is deduced from the geometric model. The equations of the choked flow are used to compute the inlet, the outlet and the leakage mass flow rates. The model of the DC generator is introduced in order to define the electrical power produced. Finally the second law of dynamic permits to obtain the instantaneous angular acceleration from which the angular velocity and the orbital angle are gotten.

3.1 Choked flow

The theory of the simple converging nozzle is used to determine the inlet, the outlet and the leakage mass flow rates. The expansion through the nozzle is treated as an isentropic process and so a coefficient (discharge coefficient) is used to consider the irreversibilities. It is defined as the ratio between the mass flow rate of the nozzle and the mass flow rate of an ideal nozzle which expands the same working fluid from the same inlet conditions to the same outlet pressure. The equations to use are the following:

➤ For unchoked flow

$$(3.1) \quad \frac{P_{down}}{P_{up}} > \left(\frac{2}{k+1}\right)^{\frac{k}{k-1}}$$

$$(3.2) \quad \dot{m} = AC_d \rho_{up} \sqrt{\frac{2k}{k-1} RT_{up} \left[\left(\frac{P_{down}}{P_{up}}\right)^{\frac{2}{k}} - \left(\frac{P_{down}}{P_{up}}\right)^{\frac{k+1}{k}} \right]}$$

➤ For choked flow:

$$(3.3) \quad \frac{P_{down}}{P_{up}} \leq \left(\frac{2}{k+1}\right)^{\frac{k}{k-1}}$$

$$(3.4) \quad \dot{m} = AC_d \rho_{up} \sqrt{\frac{2k}{k-1} RT_{up} \left[\left(\frac{2}{k+1}\right)^{\frac{2}{k-1}} - \left(\frac{2}{k+1}\right)^{\frac{k+1}{k-1}} \right]}$$

Where:

- A is the cross-sectional area of the orifice
- P_{up} , T_{up} and ρ_{up} are the upstream pressure, temperature and density
- P_{down} is the downstream pressure
- k is the ratio between the specific heat at constant pressure and that at constant volume
- C_d is the discharge coefficient.

3.1.1 Inlet flow

➤ For unchoked flow:

$$(3.5) \quad \frac{P_1}{P_{in}} > \left(\frac{2}{k+1}\right)^{\frac{k}{k-1}}$$

$$(3.6) \quad \dot{m}_{in} = A_{in} C_d C_{area} \rho_{in} \sqrt{\frac{2k}{k-1} RT_{in} \left[\left(\frac{P_1}{P_{in}}\right)^{\frac{2}{k}} - \left(\frac{P_1}{P_{in}}\right)^{\frac{k+1}{k}} \right]}$$

➤ For choked flow:

$$(3.7) \quad \frac{P_1}{P_{in}} \leq \left(\frac{2}{k+1}\right)^{\frac{k}{k-1}}$$

$$(3.8) \quad \dot{m}_{in} = A_{in} C_d C_{area} \rho_{in} \sqrt{\frac{2k}{k-1} RT_{in} \left[\left(\frac{2}{k+1}\right)^{\frac{2}{k-1}} - \left(\frac{2}{k+1}\right)^{\frac{k+1}{k-1}} \right]}$$

Where:

- $A_{in} = \pi R_{in}^2$ is the cross-sectional area of the inlet hole
- P_{in} , T_{in} and ρ_{in} are the inlet pressure, temperature and density
- P_1 is the chamber 1 pressure
- $k = \frac{c_p}{c_v}$
- C_d is the discharge coefficient
- C_{area} is the percentage of the inlet area that is not obstructed by the orbiting scroll tip.

In Figure 3.1 are collected some images to look at the intake area at different orbital angles.

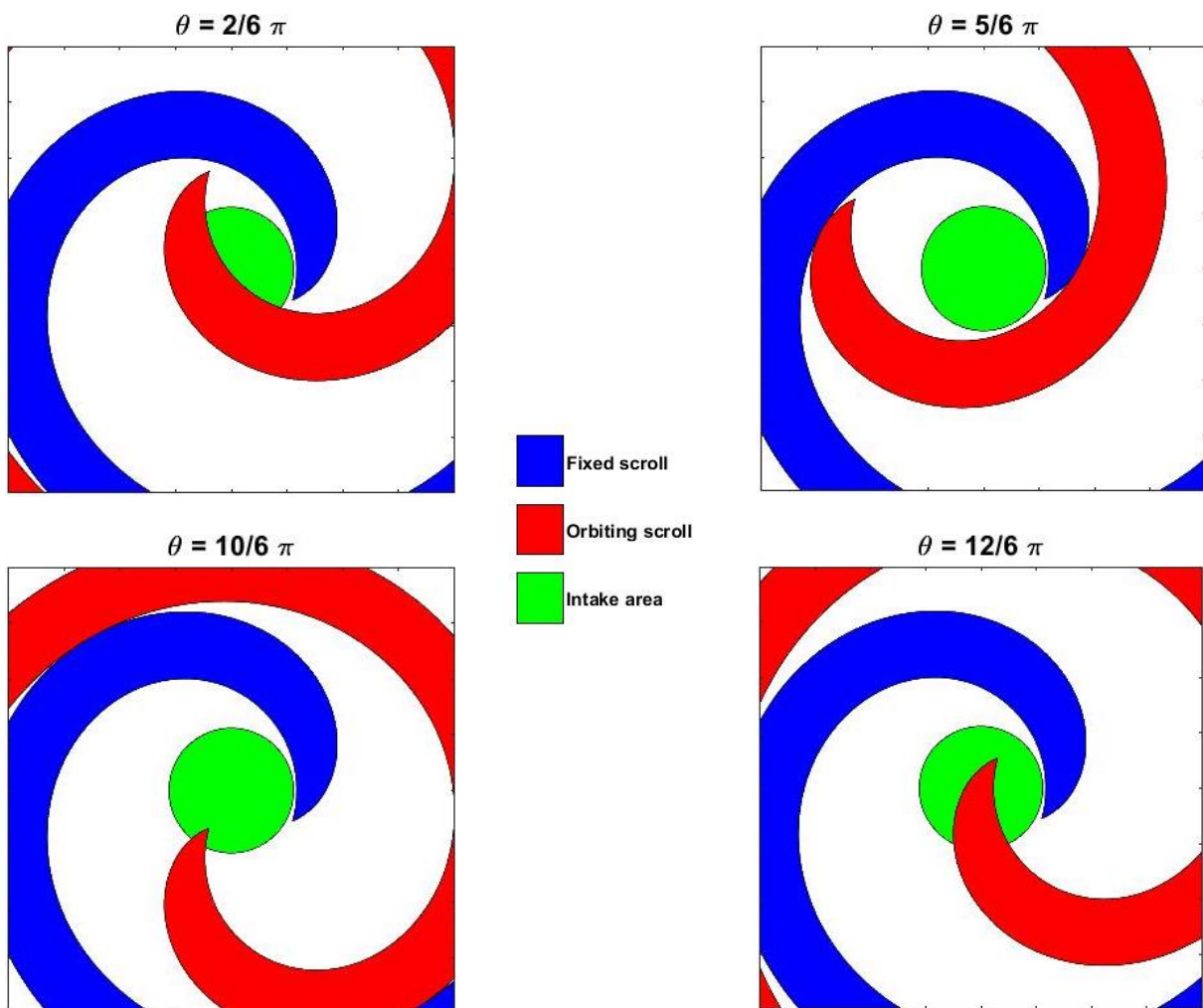


FIGURE 3.1 OBSTRUCTION OF THE ORBITING SCROLL TIP AT DIFFERENT ORBITAL ANGLES

To obtain the function represented in Figure 3.2 has been written a matlab code to depict the two spirals at different orbital angles (as in Figure 3.1). In this way it has been possible to estimate the percentage of obstacle-free entrance area. Varying the orbital angle have been found the point A in which the obstruction is maximum, the point B in which the intake area begins to be completely free and the point C in which C_{area} starts to decrease. The function is gotten joining these points with straight lines. This is an approximation but accounts quite well the orbiting spiral blockage. Finally the mathematical function has been constructed in order to get the coefficient C_{area} for all the orbital angles.

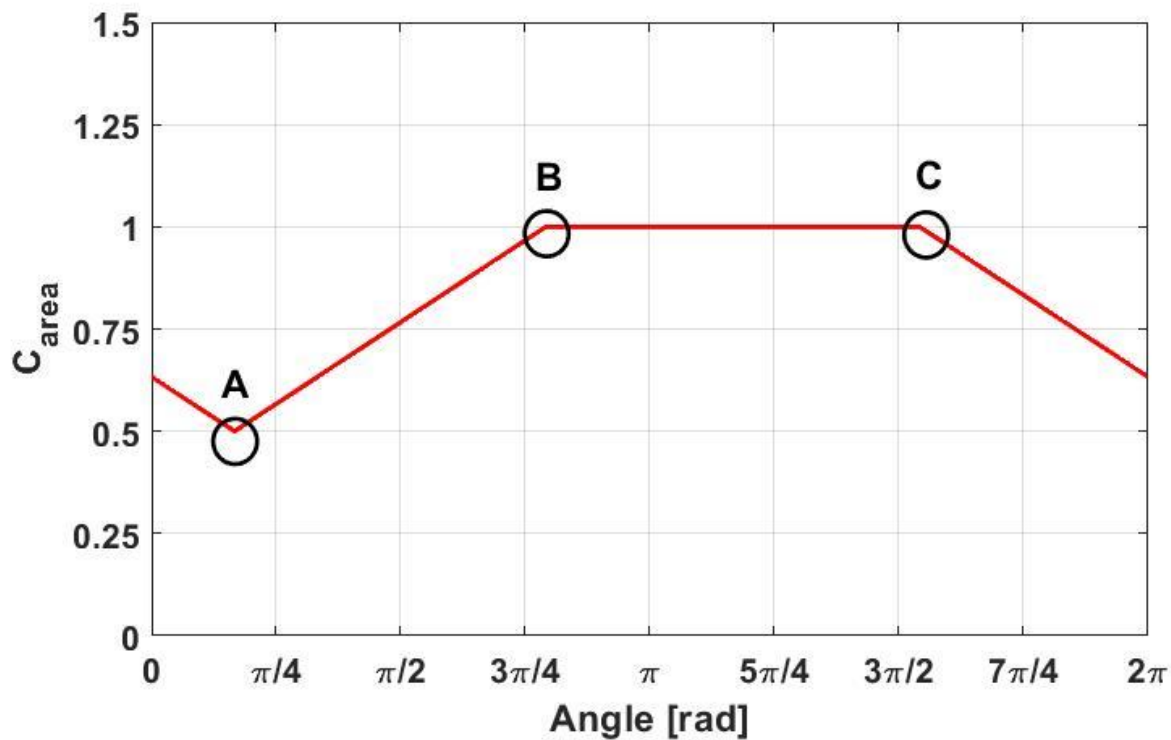


FIGURE 3.2 C_{area} AS A FUNCTION OF ϑ

3.1.2 Outlet flow

➤ For unchoked flow:

$$(3.9) \quad \frac{P_{amb}}{P_{dis}} > \left(\frac{2}{k+1}\right)^{\frac{k}{k-1}}$$

$$(3.10) \quad \dot{m}_{out} = A_{out} C_d \rho_{dis} \sqrt{\frac{2k}{k-1} RT_{dis} \left[\left(\frac{P_{amb}}{P_{dis}}\right)^{\frac{2}{k}} - \left(\frac{P_{amb}}{P_{dis}}\right)^{\frac{k+1}{k}} \right]}$$

➤ For choked flow:

$$(3.11) \quad \frac{P_{amb}}{P_{dis}} \leq \left(\frac{2}{k+1}\right)^{\frac{k}{k-1}}$$

$$(3.12) \quad \dot{m}_{out} = A_{out} C_d \rho_{dis} \sqrt{\frac{2k}{k-1} R T_{dis} \left[\left(\frac{2}{k+1}\right)^{\frac{2}{k-1}} - \left(\frac{2}{k+1}\right)^{\frac{k+1}{k-1}} \right]}$$

Where:

- A_{out} is the area of the outlet hole
- P_{dis} , T_{dis} and ρ_{dis} are the pressure, temperature and density of the discharge chamber
- P_{amb} is the ambient pressure
- $k = \frac{c_p}{c_v}$
- C_d is the discharge coefficient.

3.2 Internal leakage area and leakage flow

Ideally the fixed and the orbiting spirals should touch each other perfectly during the expansion. Actually two gaps are always present: the first is called axial gap (δ_r – Figure 3.3) and is the distance between the fixed base plate and the orbiting spiral or vice versa, the second is named radial gap and is the distance between the side surfaces of the two spirals (δ_f – Figure 3.4).

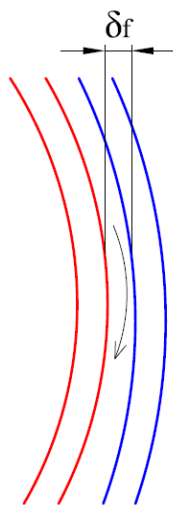


FIGURE 3.4 RADIAL GAP [8]

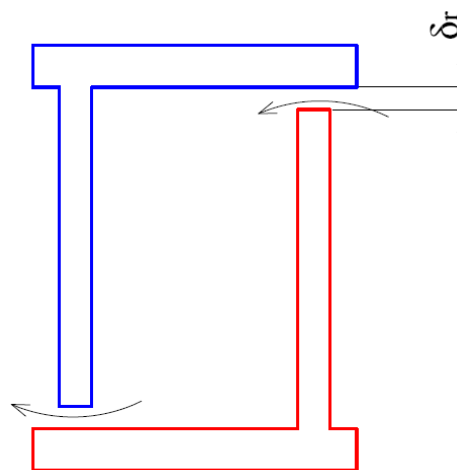


FIGURE 3.3 AXIAL GAP [8]

The radial leakages pass through the axial clearance while the flank leakages flow through the radial clearance. In the scientific literature, in most of the cases, the values assumed by axial and radial gap are constant. Rarely they are defined as functions of the pressure difference between chambers. To calculate the leakage flow is necessary to know the leak area. The two cases will be studied separately.

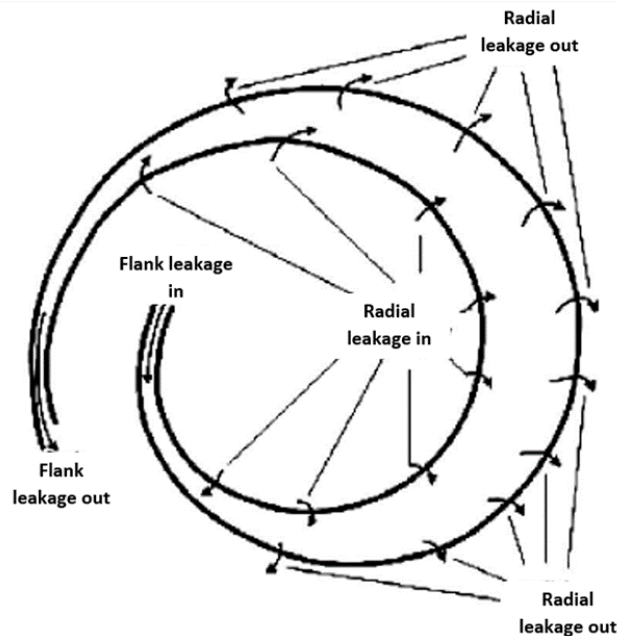
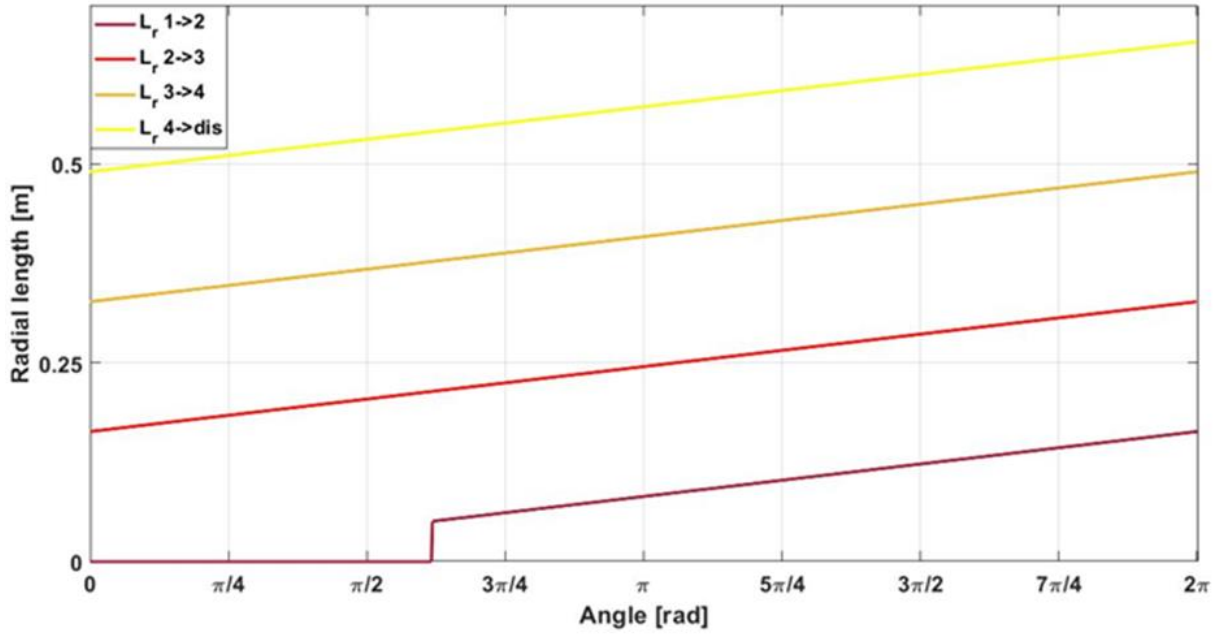


FIGURE 3.5 RADIAL AND FLANK LEAKAGE [12]

3.2.1 Radial leakage

The passage area of the radial leakage is the product between the length of the curved line between two mesh points and the axial gap. This value must be double because there are two openings for each chamber. The length of the curved line is a function of the chamber and of the orbital angle. In Figure 3.6 are shown the “radial leakage lengths” of the expander studied in this thesis. It is possible to observe that the “radial leakage length” increases with the growing of the orbital angle and the chamber considered. Regarding the first chamber is possible to see that this length is nil when the orbital angle is minor than the disconnection angle since chambers 1 and 2 are connected and so there is not a pressure difference that can produce a leakage flow. The equation 3.13 allows to calculate the “radial leakage length”:

$$(3.13) \quad L_r = 2\pi a(2(i - 1)\pi + \vartheta).$$


FIGURE 3.6 VARIATION OF THE RADIAL LENGTH

➤ For unchoked flow:

$$(3.14) \quad \frac{P_{i+1}}{P_i} > \left(\frac{2}{k+1} \right)^{\frac{k}{k-1}}$$

$$(3.15) \quad \dot{m}_{r,leak} = L_r \delta_r f_r \rho_i \sqrt{\frac{2k}{k-1} RT_i \left[\left(\frac{P_{i+1}}{P_i} \right)^{\frac{2}{k}} - \left(\frac{P_{i+1}}{P_i} \right)^{\frac{k+1}{k}} \right]}$$

➤ For choked flow:

$$(3.16) \quad \frac{P_{i+1}}{P_i} \leq \left(\frac{2}{k+1} \right)^{\frac{k}{k-1}}$$

$$(3.17) \quad \dot{m}_{r,leak} = L_r \delta_r f_r \rho_i \sqrt{\frac{2k}{k-1} RT_i \left[\left(\frac{2}{k+1} \right)^{\frac{2}{k-1}} - \left(\frac{2}{k+1} \right)^{\frac{k+1}{k-1}} \right]}$$

Where:

- δ_r is the axial gap
- P_i , T_i and ρ_i are the pressure, the temperature and the density of the i -th chamber
- P_{i+1} is the pressure of the $i+1$ -th chamber
- f_r is the flow coefficient of the radial leakage.

3.2.2 Flank leakage

The passage area of the flank leakage is the product between the spiral height and the radial gap. The height of the spiral must be considered twice because there are two openings for each chamber.

$$(3.18) \quad L_f = 2h_s$$

➤ For unchoked flow:

$$(3.19) \quad \frac{P_{i+1}}{P_i} > \left(\frac{2}{k+1}\right)^{\frac{k}{k-1}}$$

$$(3.20) \quad \dot{m}_{f,leak} = L_f \delta_f f_f \rho_i \sqrt{\frac{2k}{k-1} RT_i \left[\left(\frac{P_{i+1}}{P_i}\right)^{\frac{2}{k}} - \left(\frac{P_{i+1}}{P_i}\right)^{\frac{k+1}{k}} \right]}$$

➤ For choked flow:

$$(3.21) \quad \frac{P_{i+1}}{P_i} \leq \left(\frac{2}{k+1}\right)^{\frac{k}{k-1}}$$

$$(3.22) \quad \dot{m}_{f,leak} = L_f \delta_f f_f \rho_i \sqrt{\frac{2k}{k-1} RT_i \left[\left(\frac{2}{k+1}\right)^{\frac{2}{k-1}} - \left(\frac{2}{k+1}\right)^{\frac{k+1}{k-1}} \right]}$$

Where:

- δ_f is the radial gap
- P_i , T_i and ρ_i are the pressure, the temperature and the density of the i -th chamber
- P_{i+1} is the pressure of the $i+1$ -th chamber
- f_f is the flow coefficient for the flank leakage.

3.3 Second law of dynamics

The pressure difference between the chambers generates tangent, radial and axial forces. The tangent force is the one that produces the rotation of the orbiting scroll. This force is perpendicular to the line that connects the two basic circles centres and is towards the next chamber (the force direction is at an angle equal to $\vartheta + \frac{\pi}{2}$).

Actually only half of the wall confines with the next chamber at lower pressure. Looking at the Figure 3.7 is clear that only the part of the wall between the mesh points N and M is in contact with the pressure of the chamber 3 while the part of spiral between mesh points K and N faces an environment at the same pressure. The tangent force generated by the i -th chamber is calculated with the equation 3.23:

$$(3.23) \quad F_t(i) = 2h_s a [\vartheta + 2(i - 1)\pi](P_i - P_{i+1}).$$

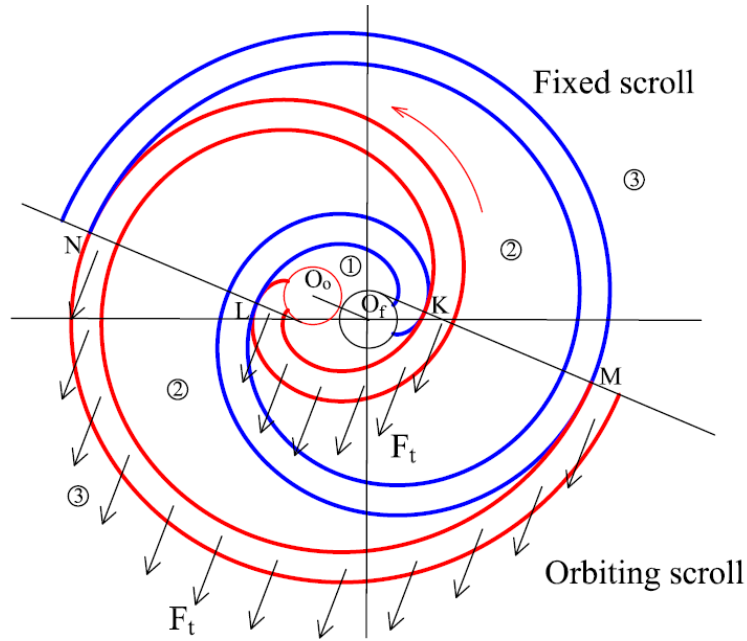


FIGURE 3.7 TANGENT FORCES [8]

Much of the radial force acting on the orbiting scroll compensates for itself. The axial force is generated by the pressure difference between the two sides of the base plates. These two forces don't have an active role in the generation of the torque but a lot of attention must be paid to balance them in order to avoid vibrations. It is also essential to avoid non-parallelism between the two plates since it can produce abrasions on the surface of the latter and so a high friction which leads to poor mechanical efficiency. In Figure 3.9 and Figure 3.8 are shown both the forces.

The torque developed by the tangent forces is calculated with the equation 3.24:

$$(3.24) \quad T_d = R_{or} \sum_{i=1}^{N_c} F_t(i).$$

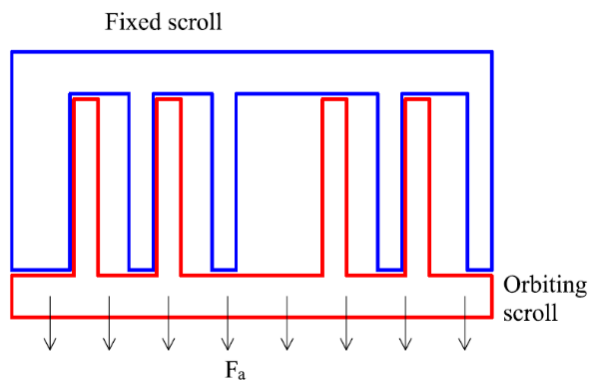


FIGURE 3.9 AXIAL FORCES [8]

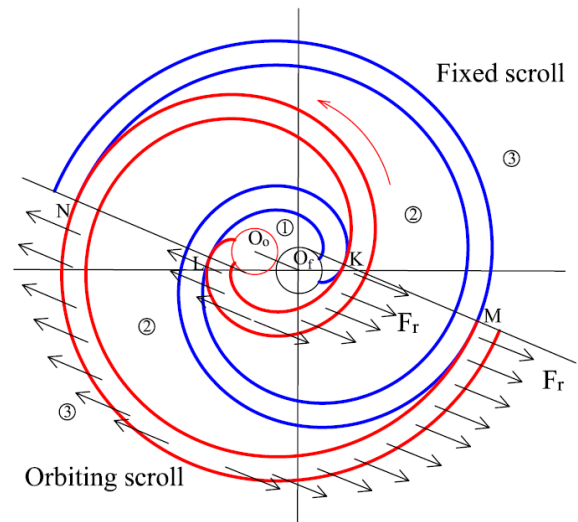


FIGURE 3.8 RADIAL FORCES [8]

At the beginning, to have motion, the driving torque must be greater than the sum between the torque requested by the DC generator and the friction torque. In steady state condition these two terms are equal. The angular acceleration is calculated with the equation 3.25:

$$(3.25) \quad (J_{orb} + J_{sha} + J_{gen}) \frac{d\omega}{dt} = T_d - T_{fr} - T_{em}$$

Where:

- $J_{orb} = m_{orb} R_{orb}^2$ is the inertia moment of the orbiting scroll
- $J_{sha} = \frac{m_{sha} R_{sha}^2}{2}$ is the inertia moment of the shaft
- J_{gen} is the inertia moment of the DC generator
- ω is the angular velocity
- T_{fr} is the torque due to the frictional forces
- T_{em} is the torque requested by the DC generator.

The angular speed is obtained integrating the angular acceleration; then, integrating the latter, the orbital angle is gotten. It is remarkable to remember that the orbital angle can vary only in the interval $0 - 2\pi$ and so, the last integral, must restart from 0 every time that the orbital angle reaches 2π .

3.4 The principle of mass conservation

To calculate the mass inside each chamber is necessary to apply the principle of mass conservation. It states that the variation over time of the mass inside a volume is equal to the difference between the inlet and the outlet mass flow rate. The expression is:

$$(3.26) \quad \frac{dm}{dt} = \dot{m}_{in} - \dot{m}_{out}.$$

For the chamber $i = 1$:

$$(3.27) \quad \frac{dm}{dt} = \dot{m}_{in} - \dot{m}_{l,out}$$

Where:

- \dot{m}_{in} is the mass flow rate that enters the expander
- $\dot{m}_{l,out}$ is the sum of radial and flank leakages going to chamber $i + 1$.

For the chamber $1 < i \leq N_C$

$$(3.28) \quad \frac{dm}{dt} = \dot{m}_{l,in} - \dot{m}_{l,out}$$

Where:

- $\dot{m}_{l,in}$ is the sum of radial and flank leakages arriving from chamber $i - 1$
- $\dot{m}_{l,out}$ is the sum of radial and flank leakages going to chamber $i + 1$.

For the chamber $i = N_C + 1$ (discharge chamber)

$$(3.29) \quad \frac{dm}{dt} = \dot{m}_{l,in} - \dot{m}_{out}$$

Where:

- $\dot{m}_{l,in}$ is the sum of radial and flank leakages arriving from chamber $i - 1$
- \dot{m}_{out} is the mass flow rate that comes out the expander.

3.5 First law of thermodynamics

To calculate the temperature and the pressure in each room is applied the first law of thermodynamics. For the next steps is important to remember the following properties of an ideal gas:

- $h = c_p T$
- $u = c_v T$
- $c_p = \frac{k}{k-1} R$
- $c_v = \frac{1}{k-1} R$
- $R = \frac{\bar{R}}{MW}$

Where:

- h is the specific enthalpy
- u is the specific internal energy
- c_p is the specific heat at constant pressure
- c_v is the specific heat at constant volume
- R is the elastic constant of the gas
- \bar{R} is the universal constant of gases (8314 J/Kmol/K)
- MW is the molecular weight.

The equation 3.30 represents the statement of the first law of thermodynamics [13] [14] [15]. All the following steps allow to get the time derivative of the chamber temperature.

$$(3.30.a) \quad \frac{d(mu)}{dt} = \dot{Q} - \dot{W} + \dot{m}_{in}h_{in} - \dot{m}_{out}h_{out}$$

$$(b) \quad \frac{d(m(h - pv))}{dt} = \dot{Q} - \frac{pdV}{dt} + \dot{m}_{in}h_{in} - \dot{m}_{out}h_{out}$$

$$(c) \quad \frac{d(mh)}{dt} - \frac{d(pV)}{dt} = \dot{Q} - \frac{pdV}{dt} + \dot{m}_{in}h_{in} - \dot{m}_{out}h_{out}$$

$$(d) \quad \frac{dm}{dt} c_p T_c + m c_p \dot{T}_c - \frac{pdV}{dt} - \frac{Vdp}{dt} = \dot{Q} - \frac{pdV}{dt} + \dot{m}_{in}h_{in} - \dot{m}_{out}h_{out}$$

$$\begin{aligned}
 (e) \quad & \frac{dm}{dt} c_p T_c + m c_p \dot{T}_c = \dot{Q} + \frac{Vd}{dt} \left(\frac{mRT_c}{V} \right) + \dot{m}_{in} h_{in} - \dot{m}_{out} h_{out} \\
 (f) \quad & \frac{dm}{dt} c_p T_c + m c_p \dot{T}_c = \dot{Q} + V \left(\frac{RT_c}{V} \dot{m} + \frac{mR}{V} \dot{T}_c - \frac{mRT_c}{V^2} \dot{V} \right) + \dot{m}_{in} h_{in} - \dot{m}_{out} h_{out} \\
 (g) \quad & \dot{m}_{in} c_p T_c - \dot{m}_{out} c_p T_c + m c_p \dot{T}_c \\
 & = \dot{Q} + V \left(\frac{RT_c}{V} \frac{dm}{dt} + \frac{mR}{V} \dot{T}_c - \frac{mRT_c}{V^2} \dot{V} \right) + \dot{m}_{in} c_p T_{in} - \dot{m}_{out} c_p T_{out} \\
 (h) \quad & \dot{m}_{in} \frac{k}{(k-1)} RT_c + m \frac{k}{(k-1)} R \dot{T}_c = \dot{Q} + RT_c \frac{dm}{dt} + mR \dot{T}_c - \frac{mRT_c}{V} \dot{V} + \dot{m}_{in} \frac{k}{(k-1)} RT_{in} \\
 (i) \quad & \dot{m}_{in} \frac{k}{(k-1)} T_c + m \frac{k}{(k-1)} \dot{T}_c = \frac{\dot{Q}}{R} + T_c \frac{dm}{dt} + m \dot{T}_c - \frac{mT_c}{V} \dot{V} + \dot{m}_{in} \frac{k}{(k-1)} T_{in} \\
 (l) \quad & m \frac{k}{(k-1)} \dot{T}_c - m \dot{T}_c = \frac{\dot{Q}}{R} + T_c \frac{dm}{dt} - \frac{mT_c}{V} \dot{V} + \dot{m}_{in} \frac{k}{(k-1)} T_{in} - \dot{m}_{in} \frac{k}{(k-1)} T_c \\
 (m) \quad & m \left(\frac{k}{(k-1)} - 1 \right) \dot{T}_c \\
 & = \frac{\dot{Q}}{R} + T_c (\dot{m}_{in} - \dot{m}_{out}) - \frac{mT_c}{V} \dot{V} + \dot{m}_{in} \frac{k}{(k-1)} T_{in} - \dot{m}_{in} \frac{k}{(k-1)} T_c \\
 (n) \quad & m \frac{1}{(k-1)} \dot{T}_c = \frac{\dot{Q}}{R} + T_c \dot{m}_{in} - T_c \dot{m}_{out} - \frac{mT_c}{V} \dot{V} + \dot{m}_{in} \frac{k}{(k-1)} T_{in} - \dot{m}_{in} \frac{k}{(k-1)} T_c \\
 (o) \quad & m \frac{1}{(k-1)} \dot{T}_c = \frac{\dot{Q}}{R} - T_c \dot{m}_{out} - \frac{mT_c}{V} \dot{V} + \dot{m}_{in} \frac{k}{(k-1)} T_{in} - \dot{m}_{in} \frac{1}{(k-1)} T_c \\
 (p) \quad & \dot{T}_c = \frac{k-1}{m} \frac{\dot{Q}}{R} - \frac{k-1}{m} T_c \dot{m}_{out} - (k-1) \frac{T_c}{V} \dot{V} + \frac{\dot{m}_{in}}{m} k T_{in} - \frac{\dot{m}_{in}}{m} T_c \\
 (q) \quad & \dot{T}_c = \frac{k-1}{m} \frac{\dot{Q}}{R} - \frac{\dot{m}_{out}}{m} k T_c - (k-1) \frac{T_c}{V} \dot{V} + \frac{\dot{m}_{in}}{m} k T_{in} - \frac{(\dot{m}_{in} - \dot{m}_{out})}{m} T_c
 \end{aligned}$$

The dot above the letters represents the time derivative of the quantity while the subscript c means “chamber”. The symbols m , p and V refer to the mass, pressure and volume of the chamber (the subscript c was omitted). In the step “g” the term $\dot{m}_{out} c_p T_c$ has been eliminated because T_c is equal to T_{out} (see Figure 3.10). In the step “e” the ideal gas state equation has been used to define the pressure. This means that from that point only substances at ideal behaviour can be used as working fluid. Different state equations, for example the virial equation, have to be introduced to consider real substances. Instead, when the working fluid is a vapour, is necessary to have some kind of software that allows to determine automatically the thermodynamics properties.

The equation that defines the time derivative of the chamber temperature is composed by five terms:

- $\frac{k-1}{m} \frac{\dot{Q}}{R} \left[\frac{K}{s} \right]$ it accounts the increasing or decreasing of the chamber temperature due to heat transfer between the rooms and towards the environment
- $\frac{\dot{m}_{out}}{m} k T_c \left[\frac{K}{s} \right]$ it accounts the increasing or decreasing of the chamber temperature due to the outlet mass flow rate
- $\frac{\dot{m}_{in}}{m} k T_{in} \left[\frac{K}{s} \right]$ it accounts the increasing or decreasing of the chamber temperature due to the inlet mass flow rate
- $\frac{(\dot{m}_{in} - \dot{m}_{out})}{m} T_c = \frac{dm}{dt} \frac{1}{m} T_c \left[\frac{K}{s} \right]$ it accounts the increasing or decreasing of the chamber temperature due to the variation of the mass inside the chamber
- $(k-1) \frac{T_c}{V} \dot{V} \left[\frac{K}{s} \right]$ it accounts the increasing or decreasing of the chamber temperature due to the variation of the chamber volume.

It is noteworthy to remember that in the first law of thermodynamics appear also the gravitational potential energy and the kinetic energy. The gravitational potential energy has been neglected because during the expansion there is not a considerable variation of the elevation. Besides the working fluid is a vapour and so it has a low density. As far as the kinetic energy is concerned the surface of the thermodynamic system has been chosen in order to have not a great difference of the velocity between the inlet and the outlet. So also the variation of kinetic energy can be omitted. Looking at the Figure 3.10 is clear that inlet and outlet mass flow rates of the i -th chamber refer to the entrance of the nozzles that simulates the leakages. This means that the velocity at the inlet and at the outlet of the thermodynamic system is not high because there is not the conversion of enthalpy in velocity.

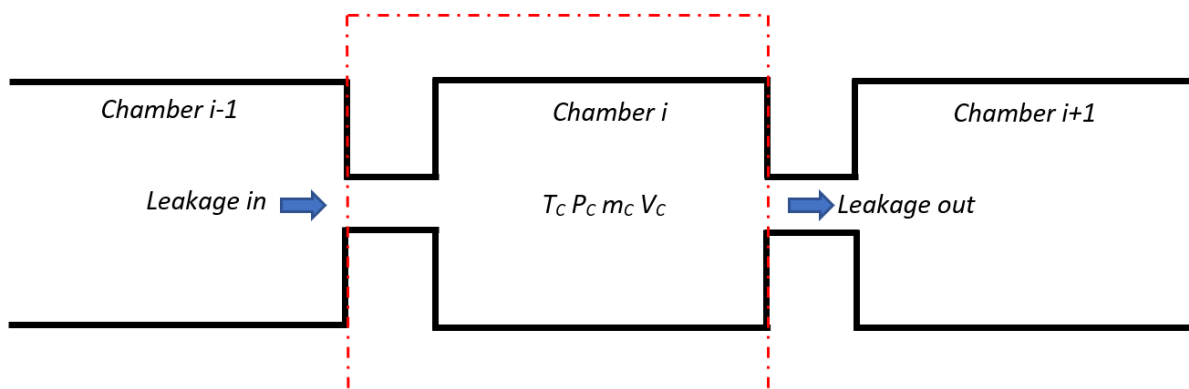


FIGURE 3.10 CONTROL SURFACE OF THE THERMODYNAMIC SYSTEM

In Figure 3.11 is shown the acceleration of the fluid between the inlet and the outlet of the nozzle. As a first approximation at the inlet we can consider a nil velocity.



FIGURE 3.11 VELOCITY BEFORE AND AFTER THE NOZZLE

In Figure 3.12 is displayed the motion of the working fluid downstream the nozzle that simulates the leakage. The control surface depicted in Figure 3.10 allows to not consider all the turbulence phenomena that occur inside the expansion chambers. It is easy to imagine that the vortices generated by the leakage flow affect strongly the convection coefficient inside the chambers.

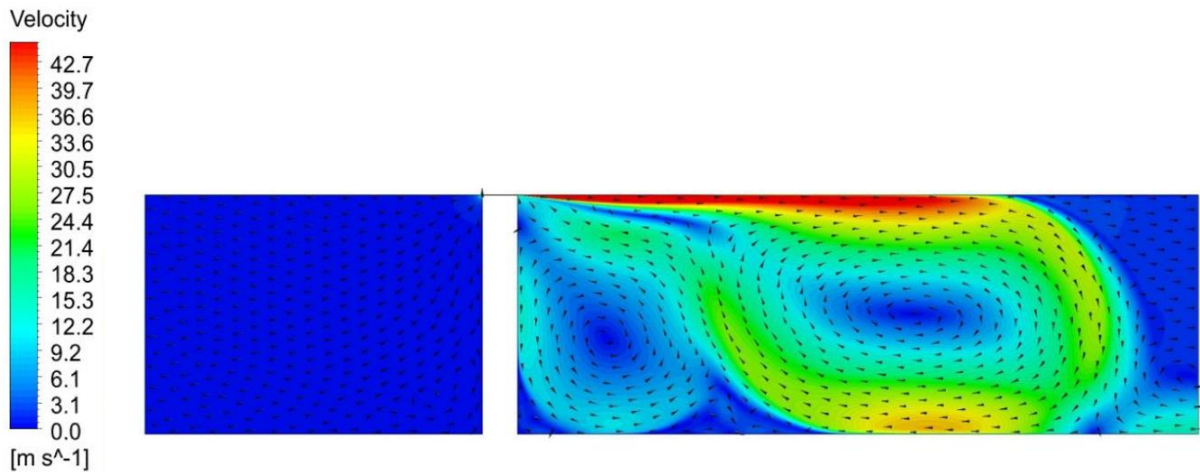


FIGURE 3.12 VELOCITY FIELD IN THE CHAMBER DOWNSTREAM OF THE NOZZLE

The term \dot{Q} is the thermal power exchanged between the working fluid and the metallic walls that enclose the chambers volume (spirals and the base plates). The value of the heat transfer coefficient inside the expansion chamber is deduced by the study of Jang and Jeong [16]:

$$(3.31) \quad Nu = \left(1 + \frac{3.5D_h}{D_c}\right) (1 + 8.8(1 - e^{-5.35St})) Nu_{DB}$$

Where:

- $Nu_{DB} = 0.023Re^{0.8}Pr^{\frac{1}{3}}$ is the Dittus-Boelter heat convection correlation
- Pr is the Prandtl number (for air 0.7)
- $Re = \frac{\rho vd}{\mu}$ is the Reynolds number (ρ is the density [kg/m^3], v is the macroscopic velocity [m/s], d is a characteristic length of the studied phenomenon [m] and μ is the dynamic viscosity [$\text{Pa}\cdot\text{s}$])
- $D_h = \frac{2R_{or}h_s}{R_{or}+h_s}$ is the hydraulic diameter
- $D_c = 2a(\vartheta + 2(i - 1)\pi)$ is the mean diameter of the scroll curvature
- $St = \frac{f_o A_{max}}{\bar{U}}$ is the Strouhal number a non-dimensional frequency factor in which $f_o = \frac{\omega}{2\pi}$ is the oscillating frequency, $\bar{U} = \frac{\dot{m}_{total}}{R_{or}h_s\rho}$ is the mean flow velocity of the working fluid and $A_{max} = R_{or}$ is the oscillating amplitude.

By neglecting the heat capacity of the spirals and base plates, the heat transfer rate into the working fluid in chamber i is [8]:

$$(3.32) \quad \dot{Q} = \frac{T_{Ci+1} - T_{Ci}}{\frac{t_s}{\lambda_s} + \frac{D_h}{Nu_{Ci+1}\lambda_{WF}} + \frac{D_h}{Nu_{Ci}\lambda_{WF}}} A_i + \frac{T_{Ci-1} - T_{Ci}}{\frac{t_s}{\lambda_s} + \frac{D_h}{Nu_{Ci-1}\lambda_{WF}} + \frac{D_h}{Nu_{Ci}\lambda_{WF}}} A_{i-1} + \frac{T_{amb} - T_{Ci}}{\frac{t_{plate}}{\lambda_{plate}} + \frac{1}{\alpha_{amb}} + \frac{D_h}{Nu_{Ci}\lambda_{WF}}} A_{pi}$$

Where:

- λ is the thermal conductivity
- t is the thickness
- The subscript s means “scroll”, WF “working fluid”, p “plate”
- α_{amb} is the natural convection heat transfer coefficient
- A_i is the area between the chambers

$$\begin{cases} A_i = 2\pi a h_s (2(i - 1)\pi + \vartheta) & i \leq N_C \\ A_i = 2\pi R_{sh} h_s & i = N_C + 1 \end{cases}$$

- $A_{pi} = \frac{2V_{Ci}}{h_s}$ is the area between chamber and base plates.

For the first chamber the second term on the right hand of the equation 3.32 vanishes while for the discharge chamber the downstream temperature T_{Ci+1} is the environment temperature and the heat transfer coefficient term $\frac{D_h}{Nu_{Ci+1}\lambda_{WF}}$ is replaced by $\frac{1}{\alpha_{amb}}$.

3.6 DC generator

In a DC (direct current) generator the mechanical power produced by a motor is transformed in direct current electricity. The two equation that govern a DC generator are [17] [18]:

$$(3.33) \quad T_{em} = K_t I_a$$

$$(3.34) \quad E_a = K_e \omega = (R_a + R_{load}) I_a + \frac{L_a dI_a}{dt}$$

Where:

- K_t is the torque constant
- I_a is the current
- E_a is the electromotive force (EMF)
- K_e is the EMF constant
- L_a is the armature inductance
- R_a is the armature resistance
- R_{load} is the resistance of the electric load.

Chapter 4

Definition of the efficiency

The scroll expanders unlike turbines are more suitable for small scale power units. Usually the pressure ratio varies from 1.25 to 10, the rotation speed from 250 rpm to 5000 rpm and the shaft power from several hundreds watt to 10 kW. The values of the isentropic efficiency that can be found in the scientific literature ranges from 40% to 80%. In Table 4.1 are gathered the results of some studies.

TABLE 4.1 [11]

Authors	Built in volume ratio	Ideal pressure ratio	Maximum shaft power [kW]	Isentropic efficiency	Working fluid
Bell et al. (2011) [19]	1.61	-	-	65%	R410a
Hugenroth et al. (2006) [20]	1.80	-	-	66%	R134a
Woodland et al. (2012) [21]	1.80	2.1	-	74%	R134a
Mendoza et al. (2014) [22] [23]	1.90	2.2/1.95	0.35/0.96	60-61%	Air/NH ₃
Kane et al. (2003) [24]	2.30	2.76	10	68%	R134a/R123
Zanelli and Favrat (1994) [25]	2.44	3.2	3.5	65%	R134a
Wang et al. (2009) [26]	2.50	3.7	1	77%	R134a
Lemort et al. (2012) [27]	3.00	3.65	2.16	71%	R245a
Feng et al. (2017) [28]	3.00	-	2.78	85%	R123
Yanagisawa et al. (2001) [29]	3.18	5.05	-	60%	Air
Yang et al. (2017) [30]	3.24	-	2.64	80%	R245fa
Qiu et al. (2018) [31]	3.50	-	0.97	58%	Air
Declaye et al. (2013) [32]	3.95	3.42/4.33	2.1	76%	R245a
Lemort et al. (2009) [33]	4.05	5.25	1.82	68%	R123
Peterson et al. (2008) [34]	4.57	3.82	0.26	50%	R123

In this thesis the analysis of the efficiency has been limited exclusively to the expander and the DC generator. In the Figure 4.1 are indicated all the losses between the inlet air power and the electrical power. To determine the maximum power that can be generated by the inlet air is necessary to introduce the concept of exergy. The exergy associated to a quantity of energy is the maximum work achievable through a device that, interacting only with the environment, uses completely the quantity of energy, realizing one or more transformations that brings the thermodynamic state of the system to the equilibrium with the environment. The device must be ideal so all the transformations are reversible. The specific exergy can be calculated with the formula [35]:

$$(4.1) \quad b = h - h_{amb} - T_{amb}(s - s_{amb})$$

That for an ideal gas becomes:

$$(4.2) \quad b = c_p \left(T - T_{amb} - T_{amb} \ln \left(\frac{T}{T_{amb}} \right) \right) + T_{amb} R \ln \left(\frac{P}{P_{amb}} \right)$$

Where:

- h is the enthalpy and s the entropy
- the subscript "amb" refers to the ambient conditions
- T and P are the temperature and the pressure.

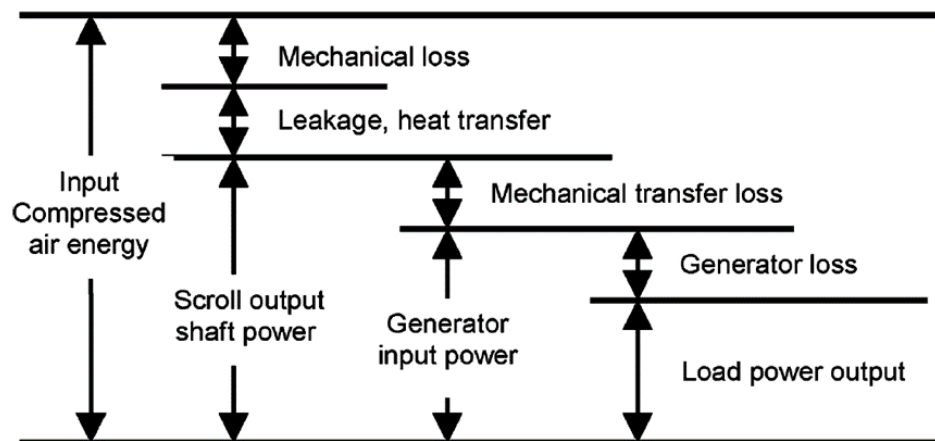


FIGURE 4.1 POWER LOSSES TO CONSIDER FOR THE PROCESS OF CONVERSION [12]

Not all the power of the inlet air is exploited by the expander because outlet pressure and temperature are not perfectly equal to those of the environment and the expansion is not reversible. In this thesis the efficiency will be defined:

$$(4.3) \quad \eta(t_1, t_2) = \frac{\int_{t_1}^{t_2} P_{out} dt}{\int_{t_1}^{t_2} P_{in} dt}$$

Where:

- t_1 and t_2 are the initial and final time instants
- P_{in} and P_{out} the inlet and outlet power.

Looking at the equation 4.3 is clear that the efficiency is defined in energy terms and not in power terms.

The isentropic efficiency is defined as:

$$(4.4. a) \quad \eta_{is} = \frac{\int_{t_1}^{t_2} (h_{in} \dot{m}_{in} - h_{out} \dot{m}_{out}) dt}{\int_{t_1}^{t_2} (h_{in} \dot{m}_{in} - h_{out, is} \dot{m}_{out}) dt}$$

$$(b) \quad \eta_{is} = \frac{\int_{t_1}^{t_2} (c_p T_{in} \dot{m}_{in} - c_p T_{out} \dot{m}_{out}) dt}{\int_{t_1}^{t_2} (c_p T_{in} \dot{m}_{in} - c_p T_{out, is} \dot{m}_{out}) dt}$$

$$(c) \quad \eta_{is} = \frac{\int_{t_1}^{t_2} \left(\dot{m}_{in} - \frac{T_{out}}{T_{in}} \dot{m}_{out} \right) dt}{\int_{t_1}^{t_2} \left(\dot{m}_{in} - \frac{T_{out, is}}{T_{in}} \dot{m}_{out} \right) dt}$$

$$(d) \quad \eta_{is} = \frac{\int_{t_1}^{t_2} \left(\dot{m}_{in} - \frac{T_{out}}{T_{in}} \dot{m}_{out} \right) dt}{\int_{t_1}^{t_2} \left(\dot{m}_{in} - \frac{P_{in}^{\frac{1-k}{k}}}{P_{out}^{\frac{1-k}{k}}} \dot{m}_{out} \right) dt}$$

In step “d” was used the equation of the isentropic process $\left(TP^{\frac{1-k}{k}} = cost \right)$.

The scroll efficiency considers all the losses inside the expander i.e. friction, air leaks and the thermal exchange. It can be calculated with the following equation:

$$(4.6. a) \quad \eta_s = \frac{\int_{t_1}^{t_2} P_{sha} dt}{\int_{t_1}^{t_2} P_s dt}$$

$$(b) \quad \eta_s = \frac{\int_{t_1}^{t_2} T \omega \eta_{mec} dt}{\int_{t_1}^{t_2} (\dot{m}_{in} c_p T_{in} - \dot{m}_{out} c_p T_{out}) dt}$$

In which:

- The term η_{mec} is defined in the paragraph 4.2
- T is the torque generated by the expander
- ω is the angular velocity.

The generator efficiency is defined as:

$$(4.7.a) \quad \eta_{gen} = \frac{\int_{t_1}^{t_2} P_{load} dt}{\int_{t_1}^{t_2} (P_{generator} + P_{ecc}) dt}$$

$$(b) \quad \eta_{gen} = \frac{\int_{t_1}^{t_2} R_{load} I_a^2 dt}{\int_{t_1}^{t_2} (T\omega\eta_{mec} + R_{ecc} I_{ecc}^2) dt}$$

Where:

- $P_{generator}$ is equal to P_{shaft} because the transmission is supposed with an efficiency equal to 1
- P_{ecc} is the power required by the excitation winding to generate the magnetic field
- R_{ecc} and I_{ecc} are the resistance and the current of the excitation winding.

The last efficiency defined is the exergetic efficiency:

$$(4.8.a) \quad \eta_{ex} = \frac{\int_{t_1}^{t_2} T\omega\eta_{mec} dt}{\int_{t_1}^{t_2} (\dot{m}_{in} b_{in} - \dot{m}_{out} b_{out}) dt}$$

The latter is the ratio between the actual mechanical energy produced to the shaft and the theoretical maximum energy that could be generated by an ideal device exploiting the difference between inlet and outlet air thermodynamic conditions.

4.1 Over\nder-expansion

Regarding inlet pressure is important to avoid under and over expansion phenomenon. In many studies it has been demonstrated (Table 4.1) that the maximum isentropic efficiency is achieved when the pressure ratio is little greater than the built-in volume ratio. In Figure 4.3 and Figure 4.2 are shown over- and under-expansion. The segments A-B, B-C, and C-D-E represent respectively suction, expansion and discharge phase. The term p_h represents the suction pressure, p_x the pressure in the last expansion chamber at the end of the expansion and p_a

the ambient pressure. We talk of under-expansion when p_x is greater than the ambient pressure; this has a negative effect on the conversion because not all the power in the inlet pressurized air is utilized. The over-expansion, in reverse, happens when p_x is lower than the ambient pressure, this causes a back flow during the discharge process. Over-expansion is particularly detrimental to the scroll expander efficiency [11].

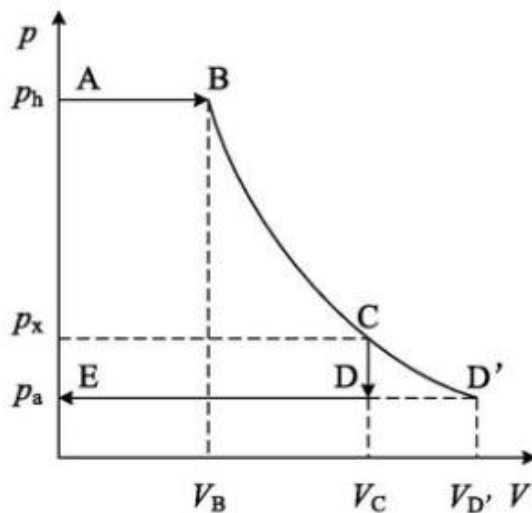


FIGURE 4.3 UNDER-EXPANSION [11]

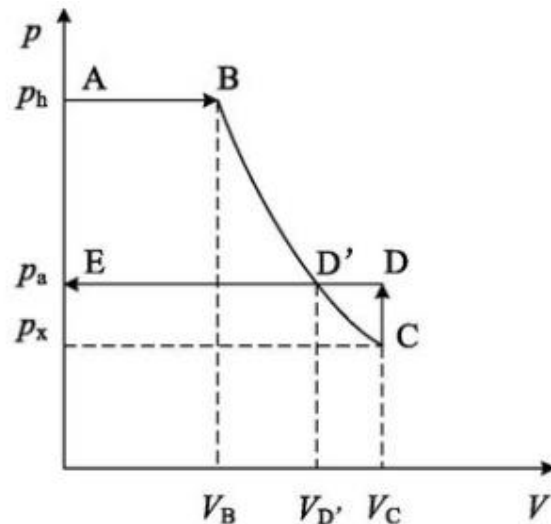


FIGURE 4.2 OVER-EXPANSION [11]

4.2 Scroll expander losses

The main losses of the expander are the heat exchanged with the environment and between the chambers, the air leaks and the friction. The first two contributions have been already considered in chapter 3. Instead, to take into account the loss due to friction, in the scientific literature, have been introduced the following equations:

$$(4.8) \quad T_{fr} = f_{sg} \omega \quad [8]$$

$$(4.9) \quad \dot{W}_{loss} = p_{me} (a\omega + b\omega^{n+1}) \quad [36]$$

Where:

- ω is the angular velocity
- T_{fr} is the friction torque
- \dot{W}_{loss} is the power lost due to friction
- a, b, f_{sg} and n are parameters to identify
- p_{me} is the internal mean effective pressure (in analogy with ICE).

To exploit these two formulations is necessary to conduct some tests to collect data and identify the parameters present in the equations. The first definition is particularly convenient because determines a torque that can be directly used in the equation of motion (equation 3.25). The second defines the power lost because of friction. The latter must be subtracted from the multiplication between the torque generated by the expander (equation 3.24) and the angular speed gettable from equation 3.25 without the term T_{fr} . These two formulations are the most precise to consider the mechanical losses because the parameters are calibrated for the specific case. In this thesis, to take into account the losses due to friction, the mechanical efficiency has been defined as follows:

$$(4.10) \quad \eta_{mec} = \frac{T_d - T_{fr}}{T_d}$$

where T_d is the drive torque and T_{fr} the friction one. In order to conform to scientific literature the mechanical efficiency has been defined as a strictly decreasing function of angular velocity. Figure 4.4 shows the mechanical efficiency as function of the angular speed.

4.3 DC generator losses

The main losses in the DC generator are:

- the copper losses due to the electrical resistance of armature and excitation winding
- the iron losses due to hysteresis and eddy currents in the iron core of the armature
- the brush losses that take place between the commutator and the carbon brushes
- the friction losses in the bearings
- the windage losses
- the stray losses that are mainly due to the armature distortion of the magnetic flux and the short circuit currents in the coil undergoing the commutation.

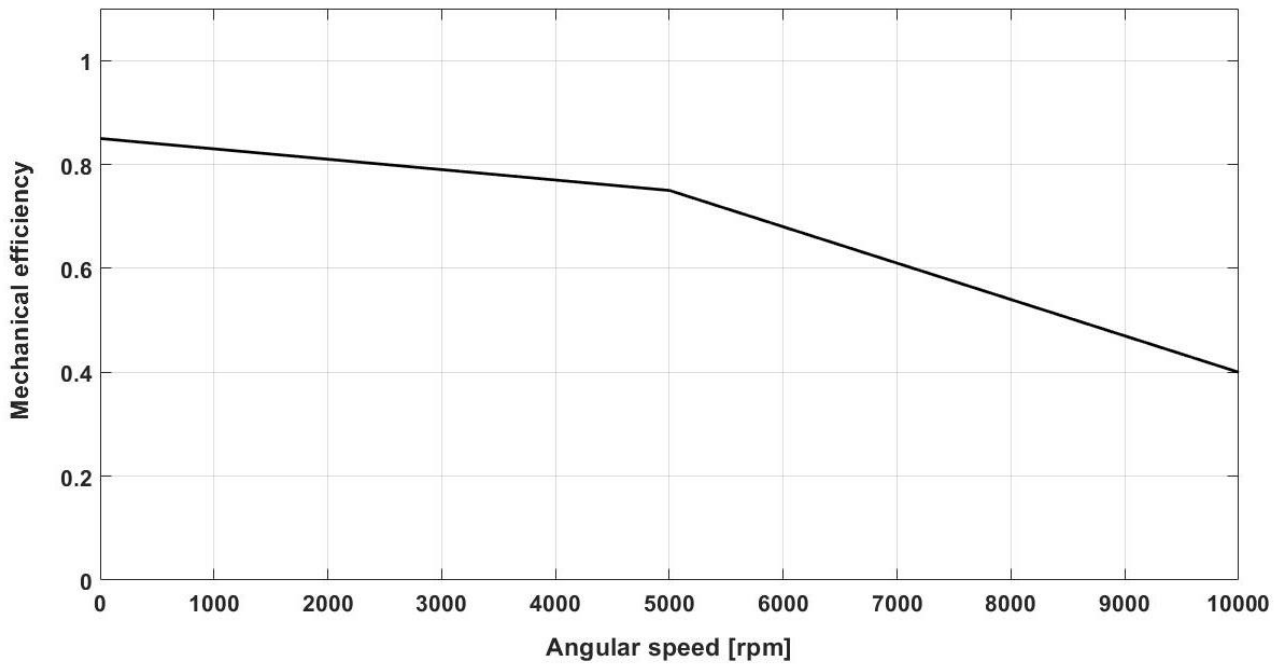


FIGURE 4.4 MECHANICAL EFFICIENCY

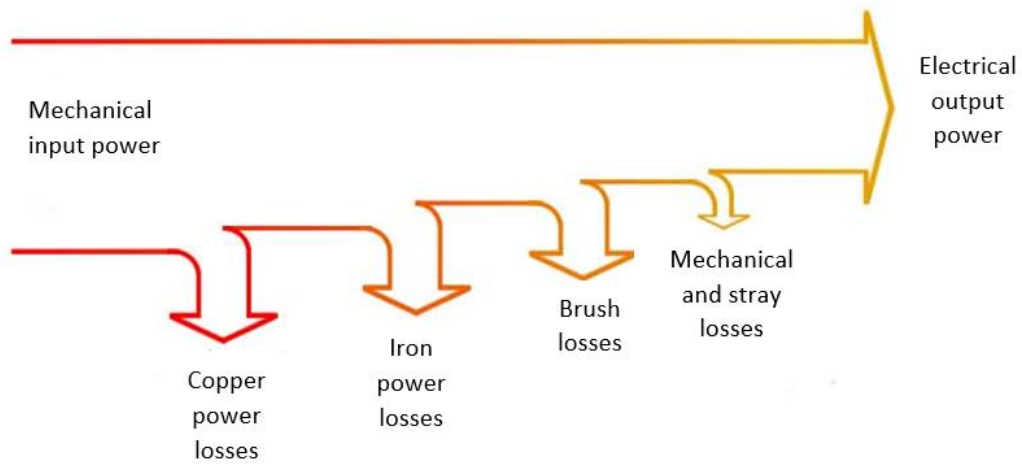


FIGURE 4.5 SANKEY DIAGRAM OF A DC GENERATOR

Chapter 5

Description of the scroll expander analysed

In this chapter are presented the data used for the simulation. Most of the geometric data can be obtained by direct measures while, a small part of them, require the use of the equations introduced in chapter 2. The data regarding the air leaks have been chosen according to the scientific literature. Lastly are presented the DC generator data that have been taken from the manufacturer's catalogue.

5.1 Spirals tips modification and gaskets

The scroll expander analysed in this thesis is a 5 kW scroll compressor operated as expander. Since some geometric values are directly measurable the expander has been disassembled.

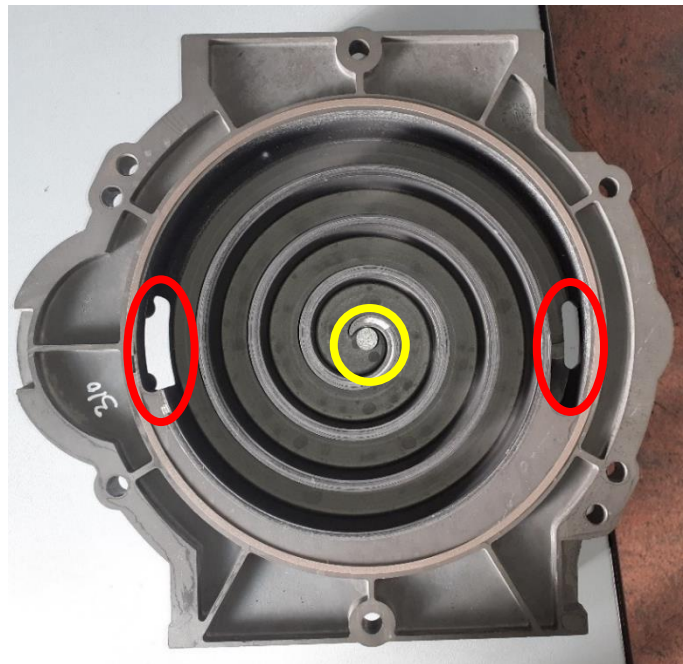


FIGURE 5.1 FIXED SCROLL STRUCTURE

In this way it has been possible to look inside the device. In Figure 5.1 is shown the structure of the fixed scroll. As can be seen the scroll tip modification is obtained by circular cutting. The two red ellipsis highlight the outlet ports while the yellow ellipse encloses the inlet port. The seals have been removed to photo them outside of their grooves. They are displayed in Figure 5.2. The outermost seal is the dustproof gasket. It has a rectangular profile and is made of PTFE with added graphite. Under the latter is positioned a tubular element made of silicone rubber (white gasket) in order to maintain the correct position of the dustproof gasket. These two seals have the objective of isolating the external environment from the internal one to the expander. The spiral seal is installed on the scroll wall in order to avoid the air leaks in radial direction. Also the latter is made of PTFE with added graphite. Moreover it is equipped with carvings as shown in Figure 5.3. The notches are designed to prevent air circulation between the expansion chambers. In fact, as soon as the expander is started, the air that tries to flow radially causes the raising of the notches. This induces the gasket to "swell" resulting in a better seal. In the orbiting scroll there is only the spiral seal.



FIGURE 5.2 FIXED SCROLL SEALS



FIGURE 5.3 NOTCHES IN THE GASKET

5.2 The geometric data

TABLE 5.1

Pit	Pitch	26	mm
t_s	Scroll thickness	6	mm
h_s	Scroll height	30	mm
N_c	Number of expansion chamber	4	
$t_{orb,disk}$	Orbiting disk thickness	6	mm
$R_{orb,disk}$	Orbiting disk radius	132	mm
R_{sha}	Shaft radius	8.3	mm
l_{sha}	Shaft length	181	mm
R_{in}	Inlet radius	5.6	mm
A_{out}	Outlet area	8.83	cm ²

TABLE 5.2

a	Basic circle radius	4.1	mm
α	Involute angle	0.72	rad
φ_e	End involute angle	26.7	rad
R_{orb}	Orbiting radius	7.0	mm
R_{sh}	Shell radius	120.6	mm
R_{mc}	Circular cutting radius	10.0	mm
V_{scroll}	Volume of the scrolls	534.82	cm ³
φ_p	Point P involute angle	0.368	rad
ϑ_{dis}	Disconnection angle	1.938	rad
γ	Geometric parameter	0.276	rad
V_{mc}	Volume removed by the circular cutting	1.03	cm ³

In Table 5.1 are collected the geometric data that can be measured directly on the spiral while in Table 5.2 are gathered the geometric values that are obtainable from the equations of the second chapter.

5.3 Properties of materials and of air

In Table 5.3 are listed the properties of the materials which the expander is made of. To simplify the study only the materials of plates, scrolls and shaft are considered. The expander analysed has the plates and the spirals made of aluminium (Al) while the shaft is made of steel (St).

TABLE 5.3

d_{Al}	Aluminium density	2700	kg/m³
λ_{Al}	Aluminium thermal conductivity	237	W/m/K
d_{St}	Steel density	8000	kg/m³
λ_{St}	Steel thermal conductivity	35	W/m/K

From the values of Table 5.1 and Table 5.3 is possible to calculate the inertia moments of the orbiting scroll and of the shaft (see Table 5.4) using the following equations:

$$(4.1) \quad m_{orb} = \left(\frac{V_{scroll}}{2} + R_{orb,disk}^2 t_{orb,disk} \pi \right) d_{Al}$$

$$(4.2) \quad m_{sha} = \pi R_{sha}^2 l_{sha} d_{st}$$

$$(4.3) \quad J_{orb} = m_{orb} R_{orb}^2$$

$$(4.4) \quad J_{sha} = \frac{m_{sha} R_{sha}^2}{2}.$$

TABLE 5.4

m_{orb}	Orbiting scroll mass	1.62	kg
m_{sha}	Shaft mass	0.31	kg
J_{orb}	Orbiting scroll inertia moment	79.5	kg mm²
J_{sha}	Shaft inertia moment	10.7	kg mm²

The working fluid used in the simulation is **DRY AIR**. This brings two advantages: the first one is that air can be approximated to an ideal gas; the second one is that air is not harmful for people and for the environment and so the tests could be conducted in more safety. It is clear that in an ORC is necessary to exploit a real substance that can evaporate and condensate. In this study the working temperature varies from $-20\text{ }^{\circ}\text{C}$ to $200\text{ }^{\circ}\text{C}$. In this interval the variation of the air thermal conductivity and viscosity can be neglected (is an approximation). The values used in this study are provided in Table 5.5.

TABLE 5.5

Pr	Prandtl number of air	0.7	
λ_{air}	Air thermal conductivity	0.026	W/m/K
μ_{air}	Air viscosity	1.8×10^{-5}	Pa s

The convective thermal coefficient for a closed environment without ventilation has been set equal to $30\text{ W/m}^2/\text{K}$.

5.4 Leakage flow data

In Table 5.6 are listed the data used to determine the air leaks between the expansion chambers and the inlet and outlet mass flow rates.

TABLE 5.6

$C_{d,in}$	Flow coefficient of the inlet mass flow rate	0.7	
$C_{d,out}$	Flow coefficient of the outlet mass flow rate	0.7	
f_f	Flow coefficient of the flank leakage mass flow rate	0.9	
f_r	Flow coefficient of the radial leakage mass flow rate	0.9	
δ_r	Axial gap	0.015	mm
δ_f	Radial gap	0.015	mm
L_f	Flank leakage "length"	60	mm

The clearance size has been reported by several studies. For example Wang et al. [12] [37] used constant values for both, 0.01 mm for the radial gap δ_f and 0.015 mm for the axial gap δ_r . Liu

et al. [38] [39] used 0.04 mm for both while Ma et al. [8] 0.01 mm. Sometimes in literature can be encounter equations in which the clearance is a function of the pressure difference between the chambers [40] [41]. Regarding the flow coefficients of the leakages Wang et al. [12] recommend a value between 0.87 and 0.95 when the working fluid is air whereas Ma et al. [8] has used 0.9 for both the flow coefficients. In this study they are set equal to 0.9. It is important to remember that the flow coefficient must be a number between 0 and 1 (1 when the flow can be assumed isentropic). Lastly, having no information about inlet and outlet flow coefficients, they have been set equal to 0.7.

5.5 DC generator

The generator is the motor LSK 1124 produced by Nidec [42] operated as generator. In the Table 5.7 are collected the data of the DC generator.

TABLE 5.7

J_{gen}	Generator inertia moment	5.3	kg dm ²
R_{arm}	Armature resistance	3.76	Ω
R_{load}	Load resistance	50	Ω
K_e	EMF constant	2.46	V*s /rad
K_t	Torque constant	2.46	Nm/A
L_a	Armature inductance	41	mH
P_{ecc}	Field power	0.65	kW

To consider the power lost due to friction in the bearings and ventilation a coefficient equal to 1.05 is multiplied by the ideal torque requested by the generator.

Chapter 6

Results of the simulation

In this chapter are shown the results of the simulation. In all the graphs in the abscissa axis is represented the time while in the ordinate axis the physical quantity analysed. The simulation duration has been set equal to 10 seconds because in this time interval all the transients extinguish and so is possible to look at the steady curves. In the charts is always present a legend in the top right corner. To have a better understanding of the graphs each room has been associated with a colour:

- Chamber 1 - **RED**
- Chamber 2 - **LIGHT BLUE**
- Chamber 3 - **PURPLE**
- Chamber 4 - **GREEN**
- Discharge chamber – **ORANGE**.

In Table 6.1 are collected the data regarding the pressures and the temperatures of inlet and outlet flows and of the environment.

TABLE 6.1

T_{in}	Inlet temperature	100	[°C]
T_{amb}	Environment temperature	20	[°C]
P_{in}	Inlet pressure	10	bar
P_{amb}	Environment pressure	1	atm
P_{out}	Outlet pressure	2	bar

The inlet pressure and temperature chosen are common in ORCs while the outlet pressure has been selected in order to have not a condensation temperature too low. Indeed, almost always, are used environmental air and water to condensate the vapor. This means that the temperature downstream of the expander must be slightly greater than that of environmental air\water. Ordinarily the condensation temperature varies from 25°C to 45°C depending on the

environmental conditions. The initial pressures and temperatures inside the expansion chambers have been set equal to those of the environment. The initial volume is obtained by the equations presented in paragraph 2.5 once the initial orbiting angle is fixed. The initial mass in the chambers is gotten from the state equation knowing the volumes, the pressures and the temperatures.

6.1 Angular speed and orbital angle

In Figure 6.1 is showed the angular speed in function of time. As can be seen after 2 seconds is reached the regime velocity. This value is strongly affected by the inlet pressure, the electrical load resistance and the torque constant of the DC generator. The initial transient is due to the inertia of orbiting scroll, shaft and generator rotor. Also the chambers pressures have a role in the initial transient. Indeed, at the begging, the pressure in the rooms is the same and so the torque generated is nil. Quickly the pressure difference between the rooms rises developing enough torque to puts in motion the expander. In Figure 6.2 the orbital angle is displayed for each time instants. The green line represents the disconnection angle. This means that when the curve is above the green line the first two chambers are separated otherwise, they are merged. In the following charts to know if the orbital angle is greater or lower than the disconnection angle is sufficient to look if in that specific instant the curve is above or under the green line.

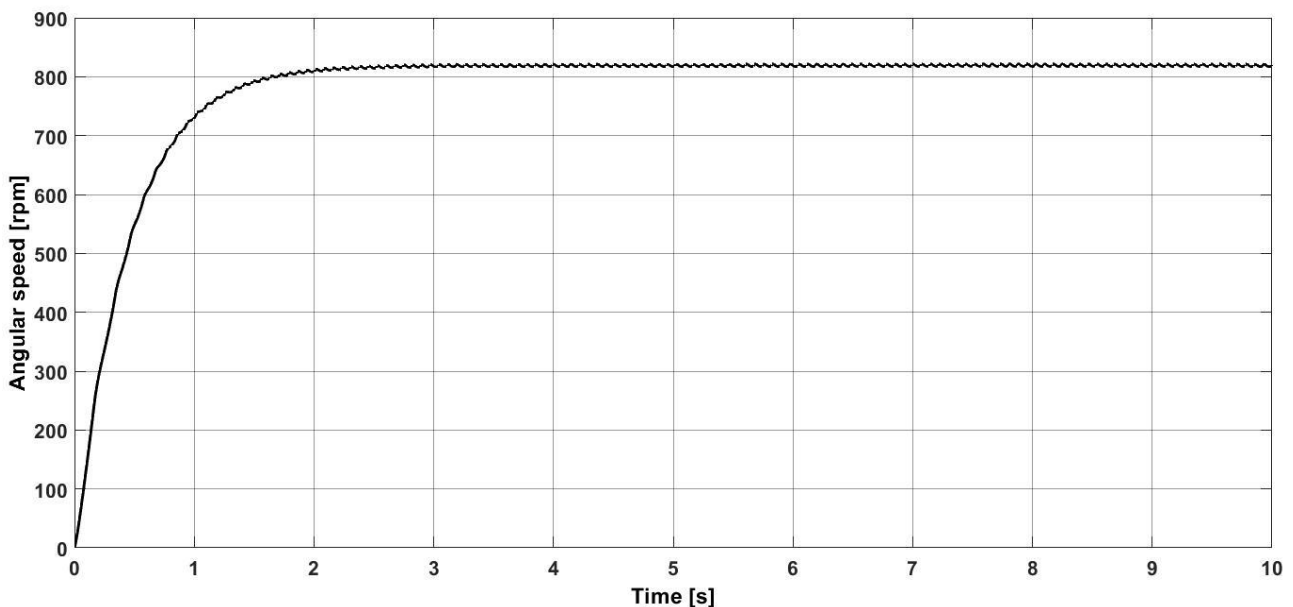


FIGURE 6.1 ANGULAR SPEED

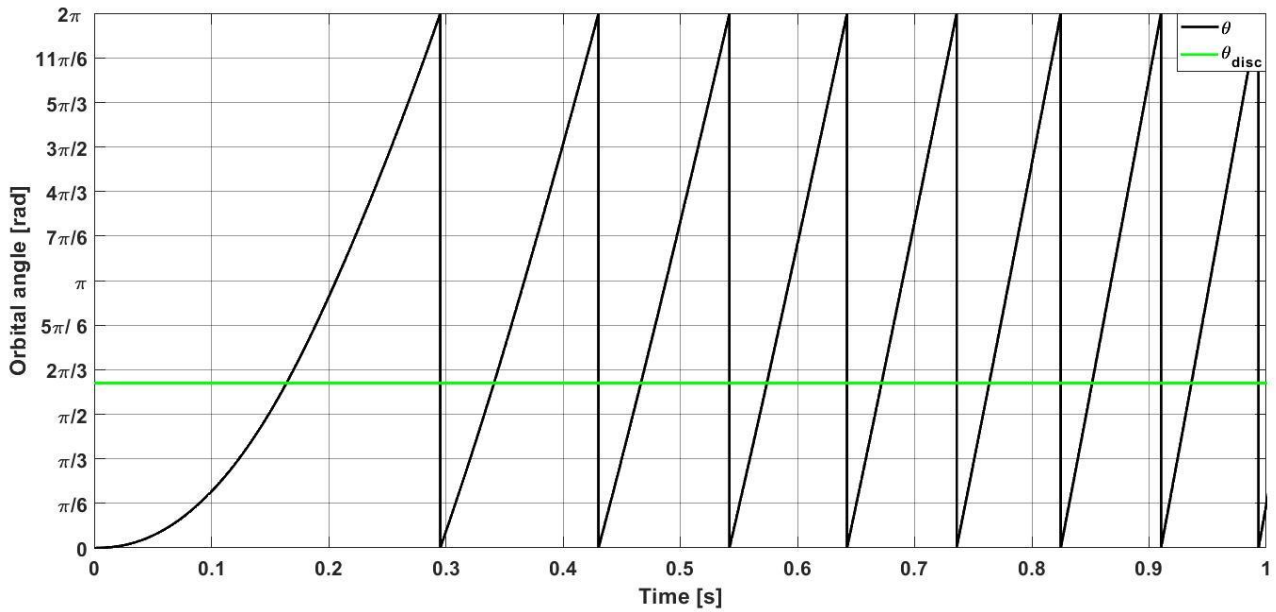


FIGURE 6.2 ORBITAL ANGLE AS A FUNCTION OF TIME

6.2 Chambers volumes

In Figure 6.4 and Figure 6.3 are shown the chambers volumes as functions of time. In all the expansion chambers the volume grows from a minimum value to a maximum. The minimum volume is reached when $\vartheta = 0 + d\vartheta$ while the maximum is obtained when the orbital angle is equal to 2π or 0. In the Figure 6.4 is highlighted the disconnection. As already said, when the orbital angle is lower than the disconnection angle, the first two rooms are linked and so is not possible to depict them separately; as soon as the disconnection angle is passed are gotten two distinct volumes. Immediately after the disconnection the second chamber volume is equal to the volume of the merged chamber minus that of the first one. As can be seen in the figure, after the disconnection, both the chambers continue to expand until the orbital angle becomes 2π . Then, with an infinitesimal increase of the orbital angle, the final volume of the chamber 2 becomes the beginning volume of the chamber 3 while the final volume of the chamber 1 turns to the beginning volume of the merge chamber. The same sequence applies to chambers 3 and 4. This means that the air pocket does not undergo to sudden expansion or compression due to the change of the chamber volume. Regarding the volume of the discharge chamber it is possible to see that it decreases with time. This is due to the fact that the shell volume is constant while the volumes of the expansion chambers grow. When the orbital angle reaches 2π the discharge chamber volume is at its minimum but, with an infinitesimal increase of the orbital angle, it rises instantaneously because the chamber 4 opens into the discharge one. In that instant the discharge chamber is at its maximum volume.

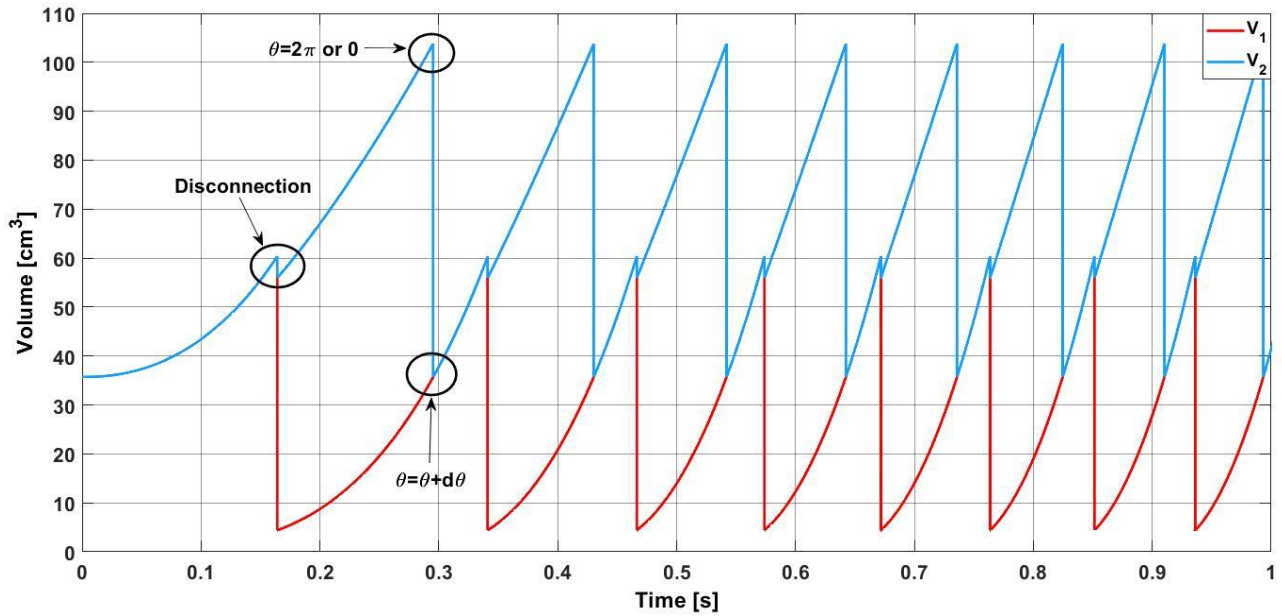


FIGURE 6.4 V_1 AND V_2

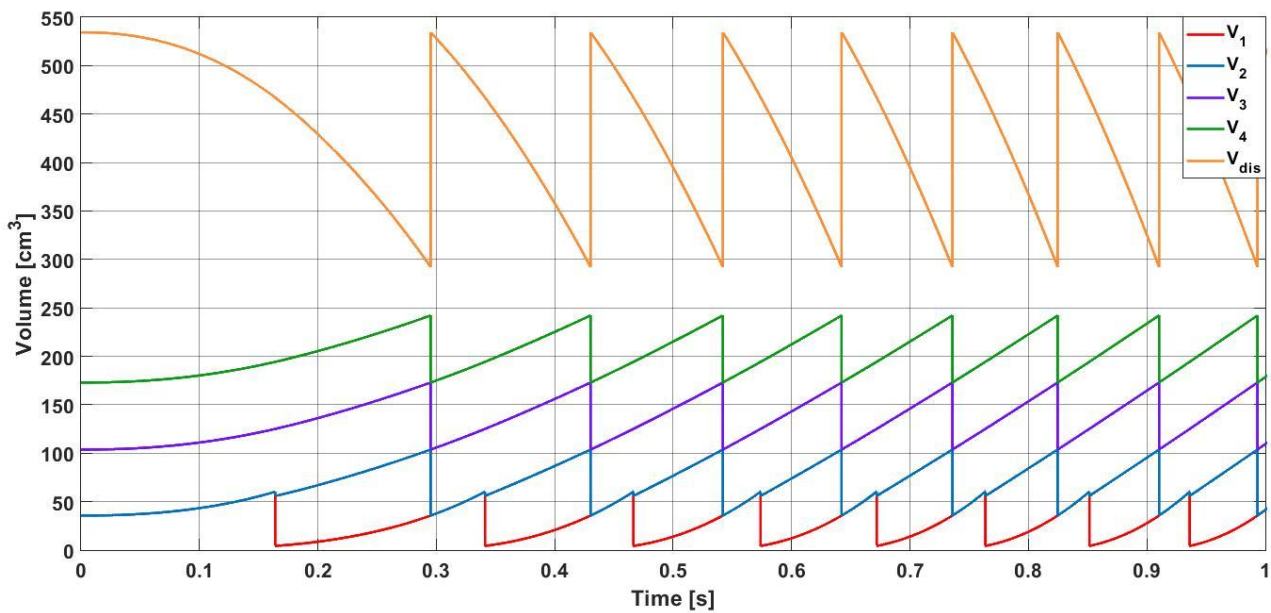


FIGURE 6.3 V_1 , V_2 , V_3 , V_4 AND V_{DIS}

6.3 Chambers pressures

In Figure 6.5 are shown the pressures of the first two chambers. As for the volumes, before the disconnection, the pressure of first and second chamber is the same because they are merged. After the disconnection only the first chamber continues to be fed by the inlet pressurized air while the inlet mass flow rate of the second chamber becomes the air leak coming from the

chamber 1. This produces a drastic reduction of the pressure in the second chamber after the disconnection because the volume continues to grow while the inlet mass flow rate remains the same. It is noteworthy the fact that the pressure in the first chamber is lightly less than the inlet pressure (10 bar). This is due to the inlet pressure drop. It is possible to see that when the coefficient C_{area} is at its minimum also the pressure in the first room is at its minimum since the inlet mass flow rate is only the 50% of its maximum (the inlet mass flow rate is directly proportional to C_{area} – see equation 3.8). In Figure 6.6 is displayed the pressure in the remaining rooms.

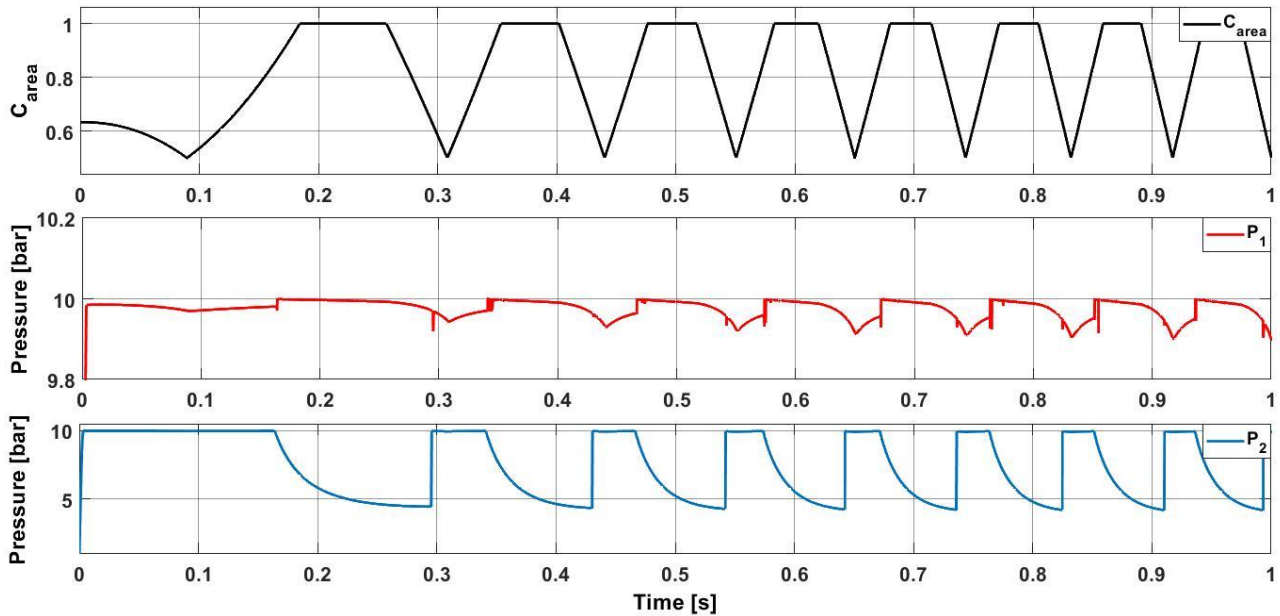


FIGURE 6.5 C_{AREA} , P_1 , P_2

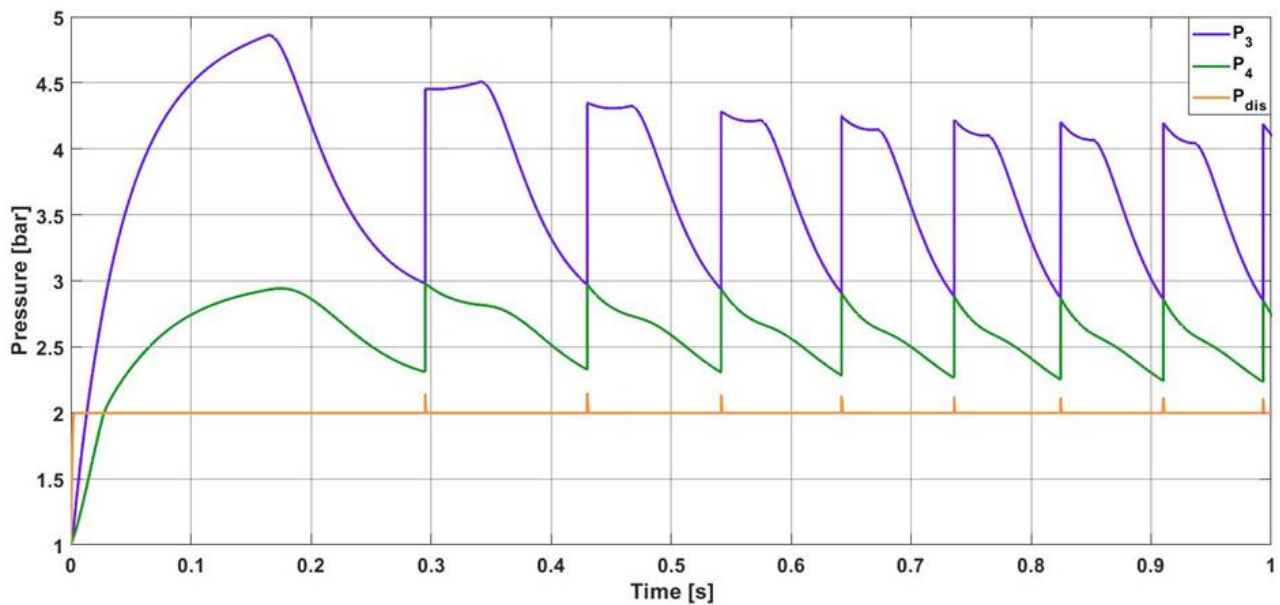


FIGURE 6.6 P_3 , P_4 , P_{DIS}

Unlike the chamber 2, the inlet mass flow rate of rooms 3 and 4 is from the beginning the air leak coming from the previous chambers. This means that the reduction of the pressure starts when ϑ is equal to 0 (for the chamber 2 the decrease starts when ϑ is equal to ϑ_{disc}). In Figure 6.7 is possible to see that P_3 does not reduce at the beginning of the cycle. This is due to the high pressure difference between chambers 2 and 3 that generates a high leakage flow that compensates the increase of the volume. When ϑ passes from 2π to $0 + d\vartheta$ the i -th room becomes the $i + 1$ th and the expansion continues without discontinuities (look at Figure 6.7). The pressure in the discharge chamber is constant over time and is equal to P_{out} . When ϑ becomes $0 + d\vartheta$ the fourth room opens inside the discharge volume inducing a slight increase of the discharge pressure. Being the outlet ports wide this peak of the pressure causes a fast rise of the outlet mass flow rate which in turn reduces rapidly the pressure in the discharge room.

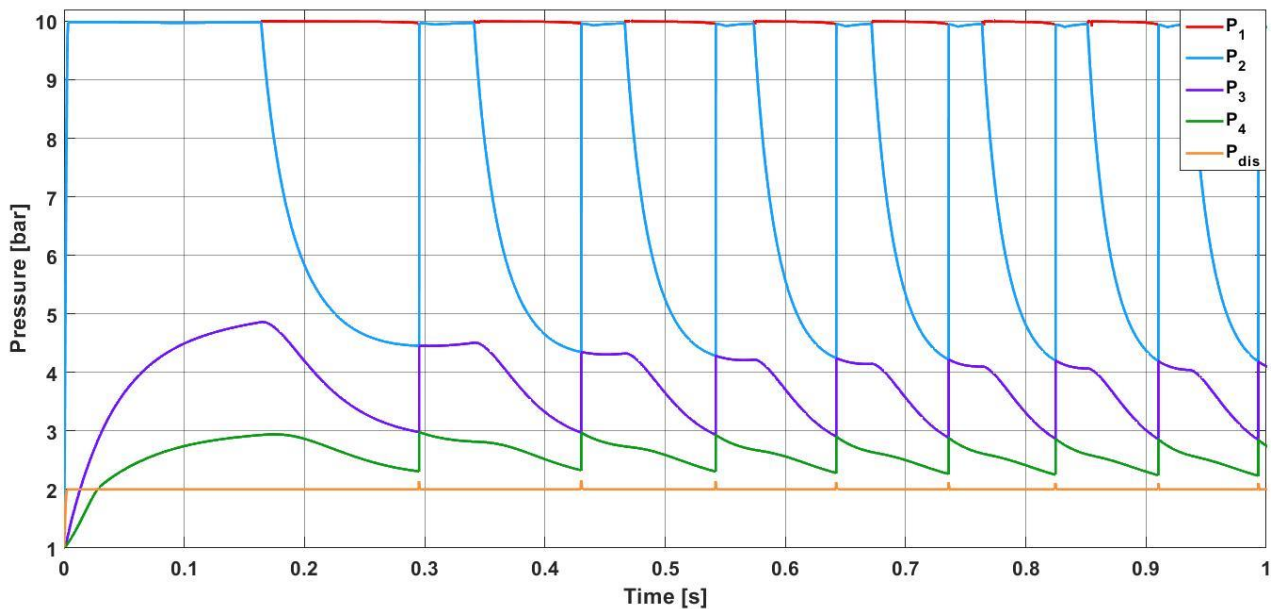


FIGURE 6.7 P_1 , P_2 , P_3 , P_4 , P_{dis}

6.4 Chambers temperature

In Figure 6.8, Figure 6.10 and Figure 6.9 are shown the temperatures inside the chambers as functions of time. The derivative of the temperature, and so the temperature itself, is gotten from the first law of thermodynamics (see equation 3.30). From that equation is possible to see that the temperature is heavily affected by the expansion and the exchange of matter and heat. It is interesting to note that at the beginning the temperatures of the first three chambers are greater than the inlet one. This is due to the fact that as soon as the valve is opened in all the expansion chambers occur an instantaneous compression. As can be seen in Figure 6.7 the

pressure in the merged room passes from 1 atm to 10 bar in less than 0.01 seconds. This generates in the first two chambers a peak of the temperature over 200 °C. The same observation can be done for rooms 3 and 4 but noting that the temperature peak is lagging behind that of the first two. This can be explained remembering that the chambers 3 and 4 are not directly connected to the inlet port and so the compression is delayed. Also the temperature manifests the same behaviour respect the orbital angle. When ϑ is lower than ϑ_{dis} the temperature of the first two rooms is the same. As soon as the disconnection angle is passed the temperature in the second room starts to decrease while that of the first chamber remains constant but slightly lower than the inlet one. This small difference of temperature is due to the thermal exchange with the environment and the second chamber. The temperature of the chamber 3 does not decrease when ϑ is lower than ϑ_{dis} because the difference of temperature between chamber 3 and chamber 1-2 is large and so a lot of heat is exchanged (remember that the spirals are made of aluminium that is an excellent thermal conductor). In Figure 6.10 are depicted the temperature of the remaining rooms. In the discharge chamber the temperature increases because the air is compressed. When ϑ becomes $0 + d\vartheta$ the fourth chamber opens into the discharge one and the two rooms air mixes. As first approximation the final temperature of the mixing can be computed with the weighted average of the temperatures respect the mass.

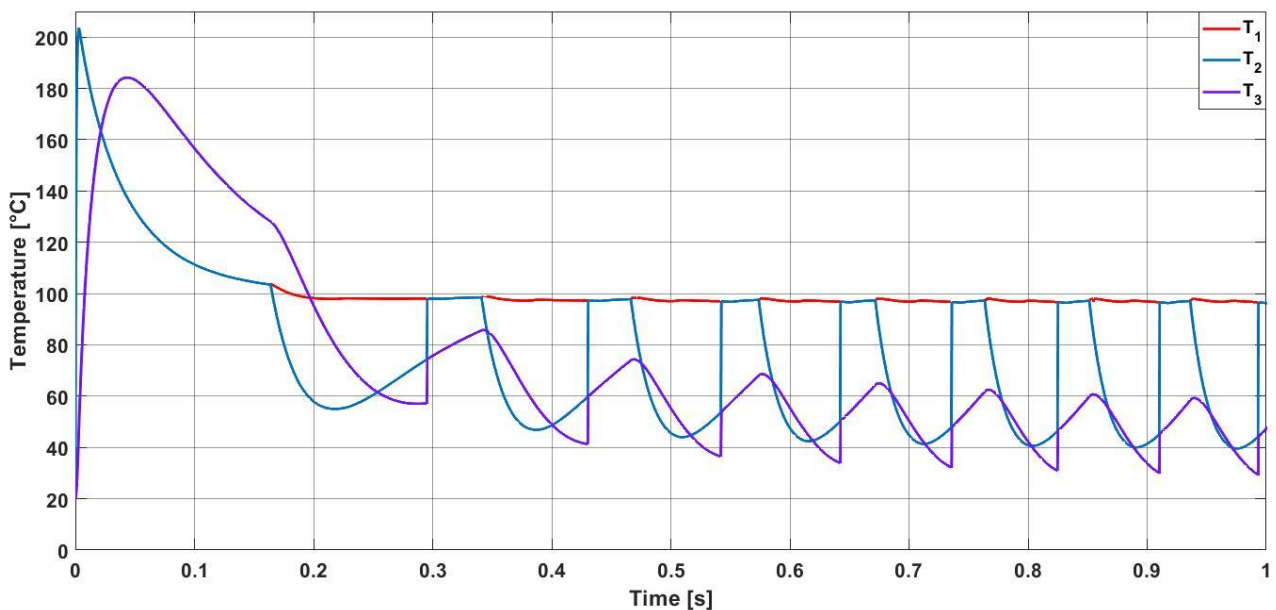


FIGURE 6.8 T₁, T₂ AND T₃

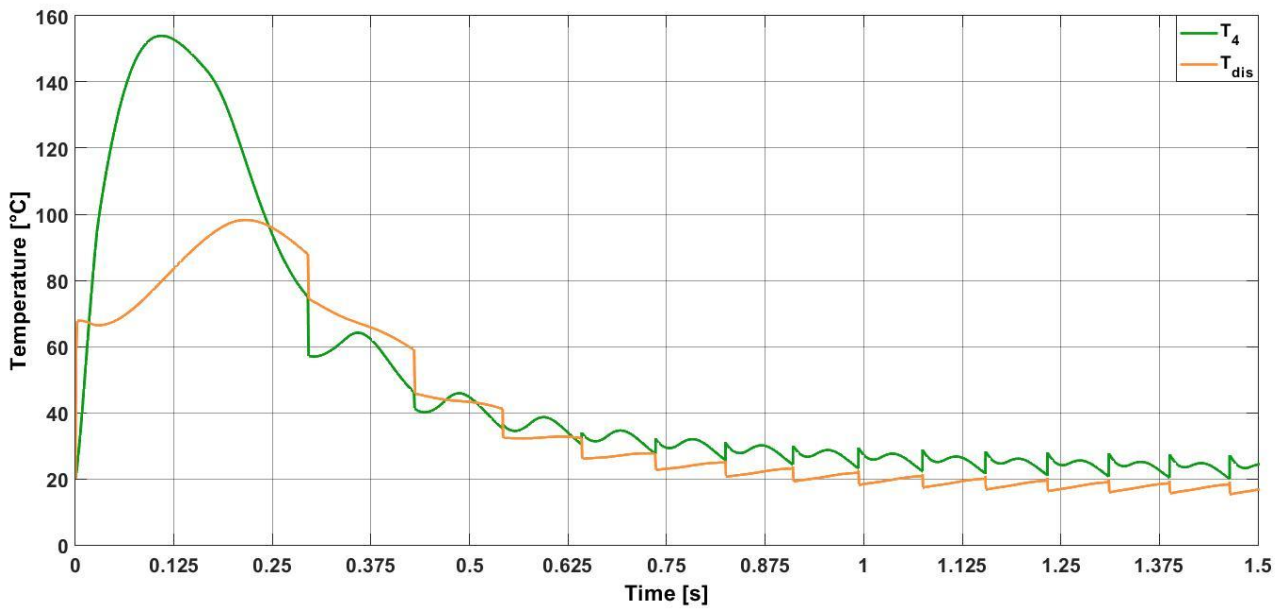


FIGURE 6.10 T_4 AND T_{dis}

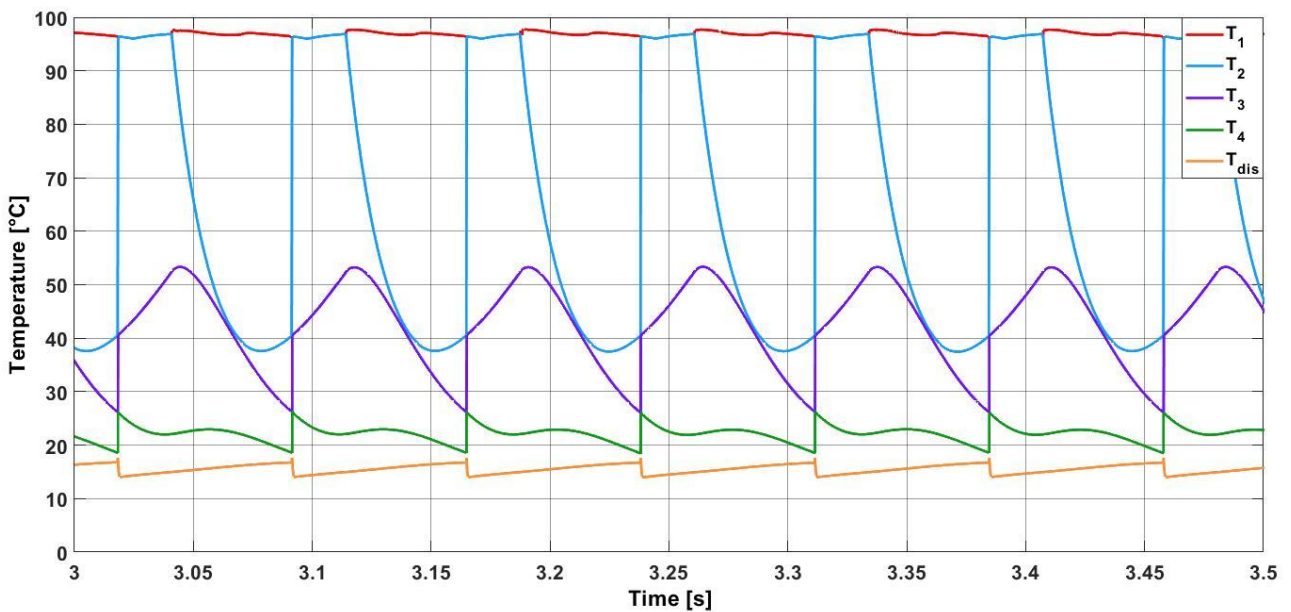


FIGURE 6.9 T_1 , T_2 , T_3 , T_4 AND T_{dis}

If total expansion had been generated by an isentropic process, the equation to use would be:

$$(6.1) \quad T_{in} P_{in}^{\frac{1-k}{k}} = T_{out} P_{out}^{\frac{1-k}{k}}$$

and so the T_{out} would be defined as:

$$(6.2) \quad T_{out} = T_{in} \left(\frac{P_{in}}{P_{out}} \right)^{\frac{1-k}{k}}.$$

Substituting T_{in} with 373 K (100°C), P_{in} with 10 bar and P_{out} with 2 bar the values of T_{out} results equal to 235 K (approximately -37°C). It is possible to notice that the outlet temperature obtained by the simulation is greater than the “isentropic” one. This is due to the fact that the real expansion is not adiabatic because the chambers exchange heat between them and with the environment. Moreover, all the irreversibilities, generate heat that warms the air. It is important to remember that the air is dry and so, with the decreasing of the temperature, there is no condensation of the water vapour.

6.5 Inlet and outlet mass flow rates

Inlet and outlet mass flow rate are shown in Figure 6.11. When ϑ becomes equal to ϑ_{disc} the inlet mass flow rate drops since the nozzles pass from 3 to 4 and so the leak stream has more difficulties to cross the expander. At the same time with the increase of the orbital angle the “length” of the radial leaks grows inducing an increment of the leakage flow and so of the inlet mass flow rate. After the discharge phase the inlet flow rate continues to rise because the nozzles return to be 3. The result of this sequence is a sawtooth curve in which the maximum is reached just before the disconnection and the minimum immediately after. As far as the outlet mass flow rate is concerned we can see in Figure 6.11 that is constant except during the discharge phase. In that brief instant it has a peak. In Figure 6.12 are depicted both the mass

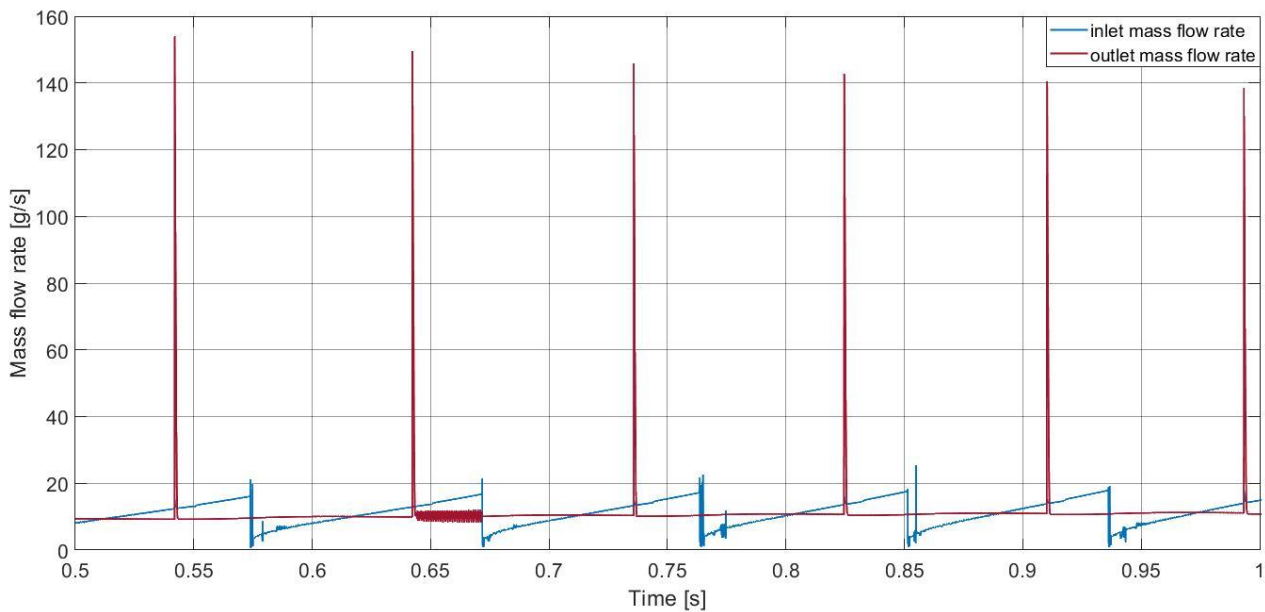


FIGURE 6.11 INLET AND OUTLET MASS FLOW RATES

flow rates in the initial instants. It is possible to see that at the beginning the inlet mass flow rate is sonic. This is correct because if we hypothesize that the critical pressure ratio is 0.5 then, until the pressure inside the first chamber is lower than 5 bar (half of the inlet pressure), the flow is sonic.

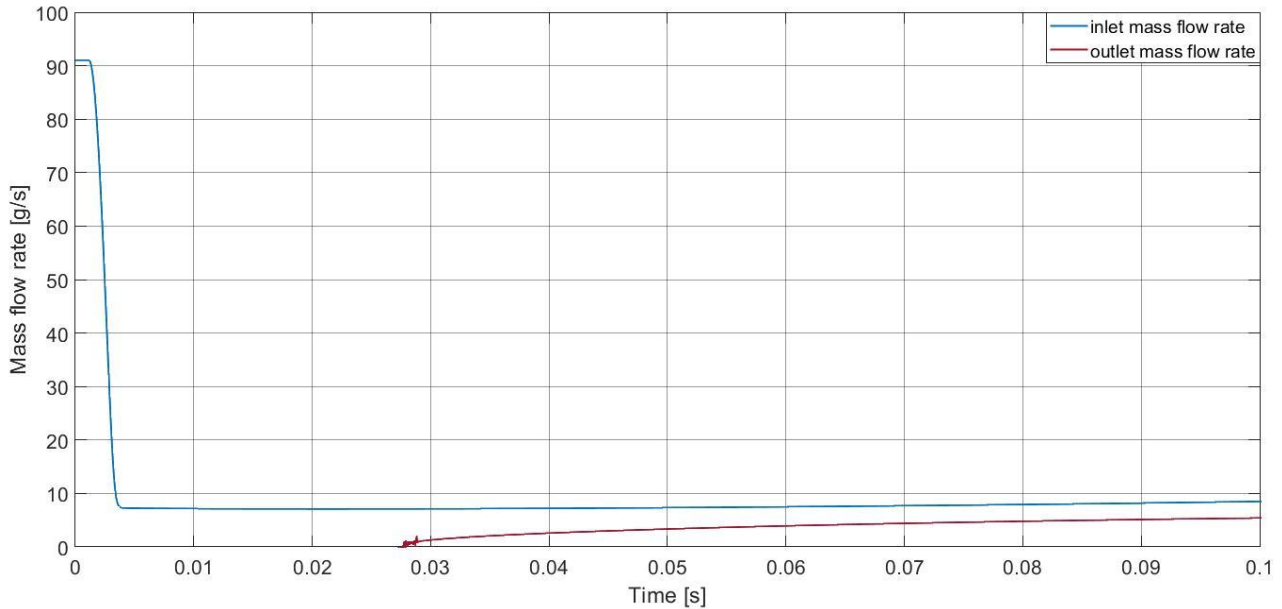


FIGURE 6.12 INITIAL INLET AND OUTLET MASS FLOW RATE

6.6 Power and Efficiencies

In Figure 6.13 are depicted the mechanical and electrical power. The difference between them is due to the efficiency of the generator. The mechanical power oscillates because the torque depends on the pressure difference between the chambers which in turn depends on the orbital angle. In Figure 6.14 are shown the angular speed and the torque separately. The efficiencies defined in chapter 4 are represented in the Figure 6.15. The initial instant of the integral has been set equal to 1 second in order to not consider the beginning transients. Neglecting the small oscillations the regime values are reported in the following table.

TABLE 6.2

η_{is}	Isentropic efficiency	61.4%
η_s	Scroll efficiency	78.8%
η_{gen}	DC generator efficiency	48.6%
η_{ex}	Exergetic efficiency	47.3%

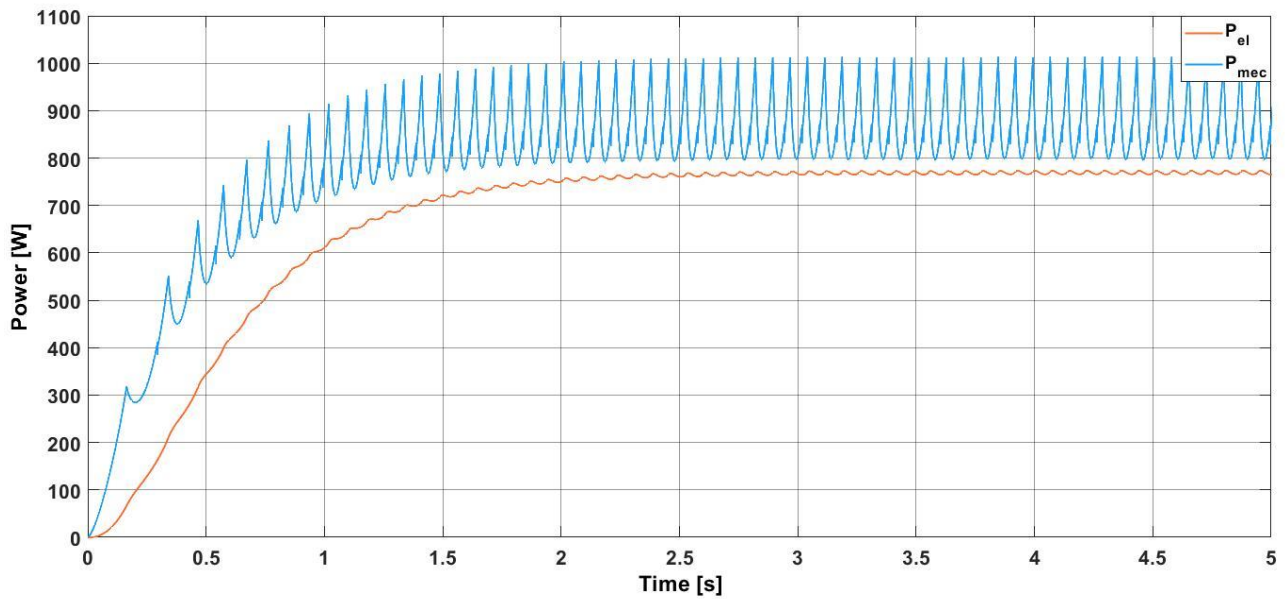


FIGURE 6.13 MECHANICAL AND ELECTRICAL POWER

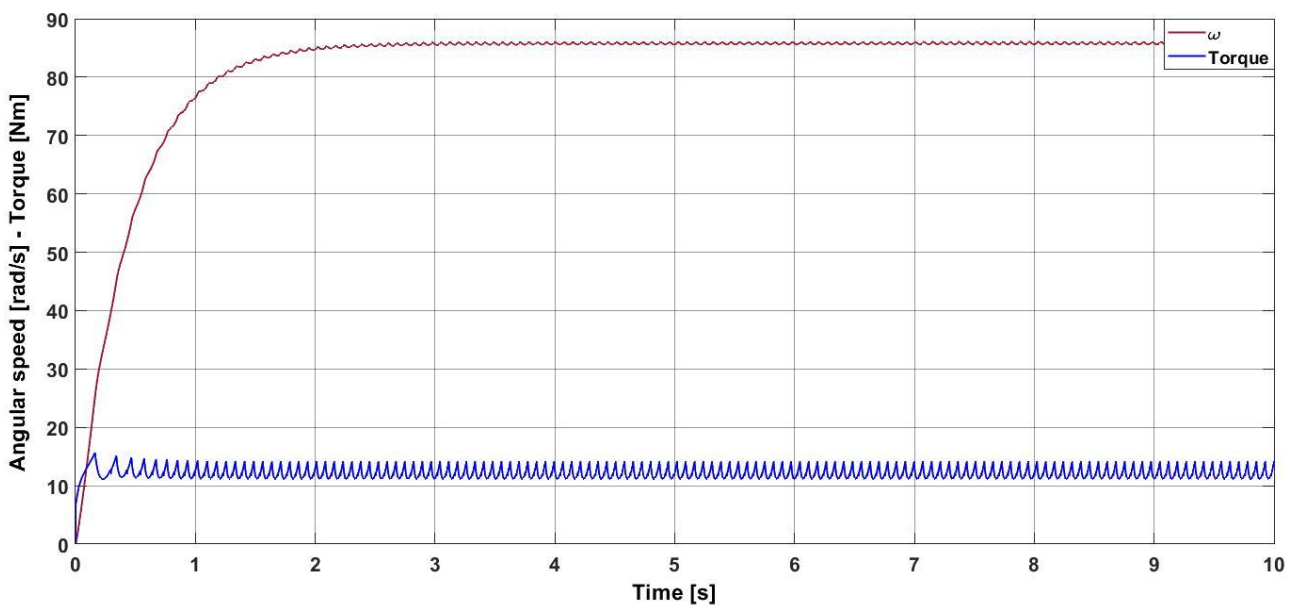


FIGURE 6.14 ANGULAR SPEED AND TORQUE

The value of the isentropic efficiency is similar to those of the Table 4.1. This value is slightly lower than that of radial and axial turbines. The latter have an isentropic efficiency between 60% and 85% based on operating conditions [43] [44] [45] [46]. The scroll efficiency displays that 22% of the enthalpy difference is lost during the conversion of the power. This loss is mainly due to heat exchange, friction and air leaks. Regarding the DC generator efficiency is possible to verify that is lower than the typical values of electrical machine because the generator chosen is not at permanent magnets. This means that is needed external electrical power to generate the magnetic field necessary to the electro-mechanical conversion. The

power required by the field winding is 650 W while the electrical power produced is slightly less than 800 W. In other words, the generator, produces approximately half of the inlet energy, namely the sum between the mechanical energy and the electrical energy needed to the generation of the magnetic field. Finally, the exergetic efficiency, shows that the expander produces 47% of the energy that could be generated exploiting the input and output temperatures and pressures listed at the beginning of the chapter.

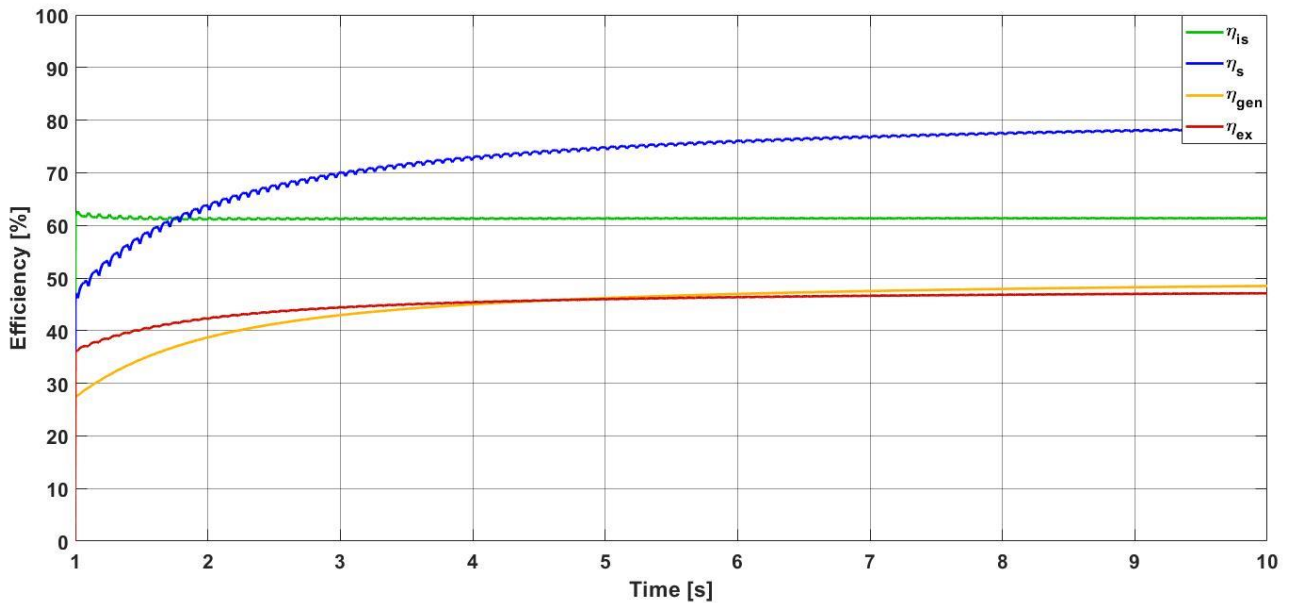


FIGURE 6.15 EFFICIENCIES

Chapter 7

Sensitivity analysis

In this chapter two sensitivity analysis are performed, one on the inlet pressure and the other on radial and axial clearances. To have a clear comprehension of the variation of results one physical quantity at time has been modified. The other data remain equal to those listed in chapter 5. The comparison is carried out between the outlet temperature, the efficiencies, the regime speed and the electrical power generated.

7.1 Inlet pressure variation

The first sensitivity analysis has been conducted on the inlet pressure. The simulated values are 7, 10, 13, 16 bar. Looking at Figure 7.1 is clear that the angular velocity grows increasing the inlet pressure. Since mechanical efficiency has a negative derivative with respect to angular velocity, passing from 7 to 16 bar its value decreases.

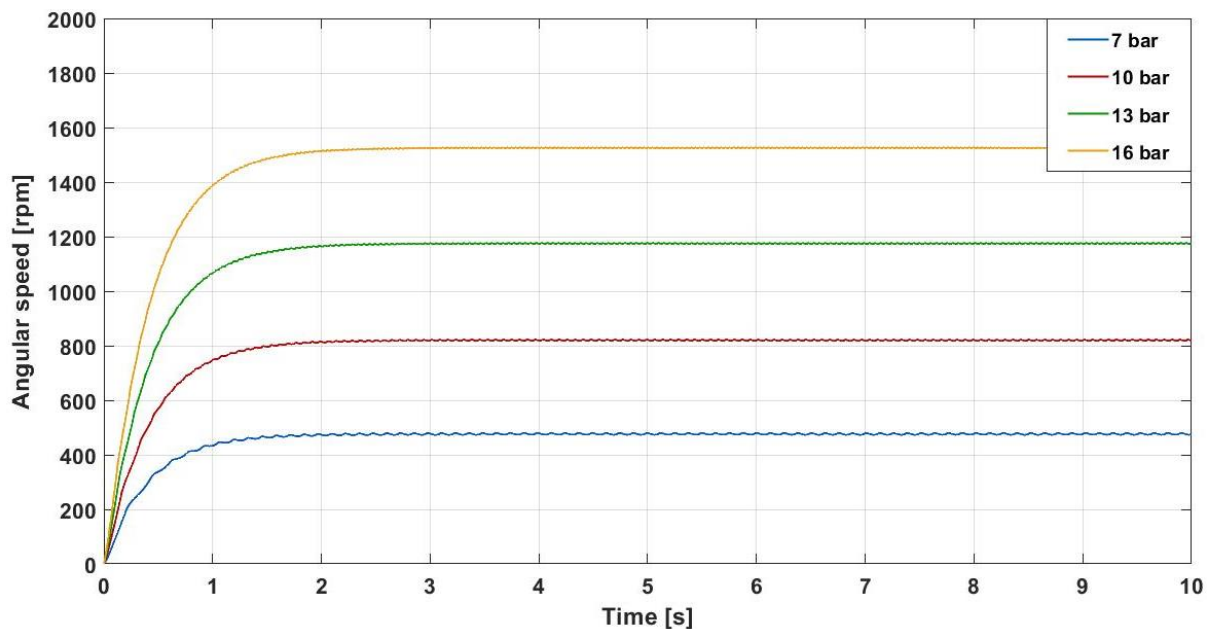


FIGURE 7.1 ANGULAR SPEED WITH DIFFERENT INLET PRESSURES

In Figure 7.2 is depicted the outlet temperature. At 13 and 16 bar the outlet temperature is negative. This is not practicable because most of the time are exploited environmental air or water to condensate the vapour after the expander. Besides, to avoid large and expensive heat exchangers, it is necessary to have a condensation temperature 15-20 °C higher than the environmental one. One solution can be to raise the inlet temperature in order to have an outlet temperature greater than that of the environment or reduce the pressure ratio.

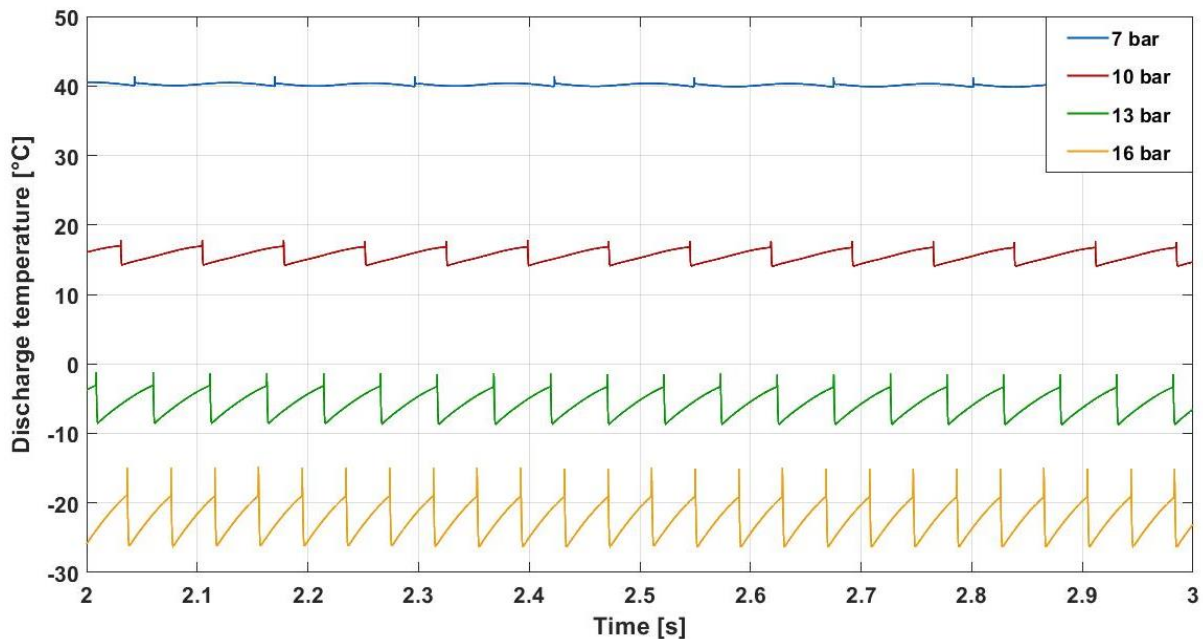


FIGURE 7.2 OUTLET TEMPERATURE WITH DIFFERENT INLET PRESSURES

In Figure 7.3 is shown the electric power produced by the generator with different inlet pressures. It is possible to see that the electric power generated is not proportional to the inlet pressure indeed, to a doubling of the inlet pressure, the electric power increases approximately nine times. This produces an increase of the generator efficiency since the power required by the excitation winding remains constant. In Table 7.1 are gathered all the efficiencies for the different inlet pressures. The variation of mechanical efficiency and that of the DC generator have been already explained. In the rows f, g, and h of the Table 7.1 are collected the heat exchanged by the chamber 1, the “frictionless” mechanical energy and the mass of air leaked from chamber 1 during the simulation. All these quantities increase passing from 7 to 16 bar. The heat is the integral over time of the algebraic sum of all the thermal powers exchanged. This means that the minus sign represents an overall thermal exchange toward the outside of the chamber. It is noteworthy that the growth rates of heat exchanged and leaked air between 7 and 16 bar are not equal to that of mechanical energy. In detail the mechanical energy produced at 16 bar is 11.18 times of that produced at 7 bar, the heat exchanged 5.53 times and the mass of leaked air 2.25 times. This causes an increase of the isentropic efficiency passing

from 7 to 16 bar because, the latter, compares the real process with the ideal one that is adiabatic and without friction and air leaks. Passing from 7 to 16 bar the actual expansion approaches to the ideal one because the heat exchanged and the mass of leaked air grow with a lower rate than that of mechanical energy. The same reasoning applies to the exergetic efficiency with the difference that the outlet temperature is the actual one and not that isentropic. Finally, the scroll efficiency increases, again, for the same reason: the numerator, the mechanical energy, grows with a rate greater than the denominator. The lower rate of grow of exchanged heat and leaked air can be explained noting that in the same simulation time, 10 seconds, the number of expansion cycles is different because the angular velocity is not the same. In this way, heat transfer and mass transfer have less time to take place as speed increases. In Table 7.2 are listed the ratios between the exchanged heat and the mechanical energy for each chamber and for all the inlet pressures. In chambers 3, 4 and in the discharge chamber the direction of the thermal flux shifts. This agrees with the reduction of the outlet temperature. In Table 7.3 are listed the ratio between the air leaked from each chamber and the mechanical energy.

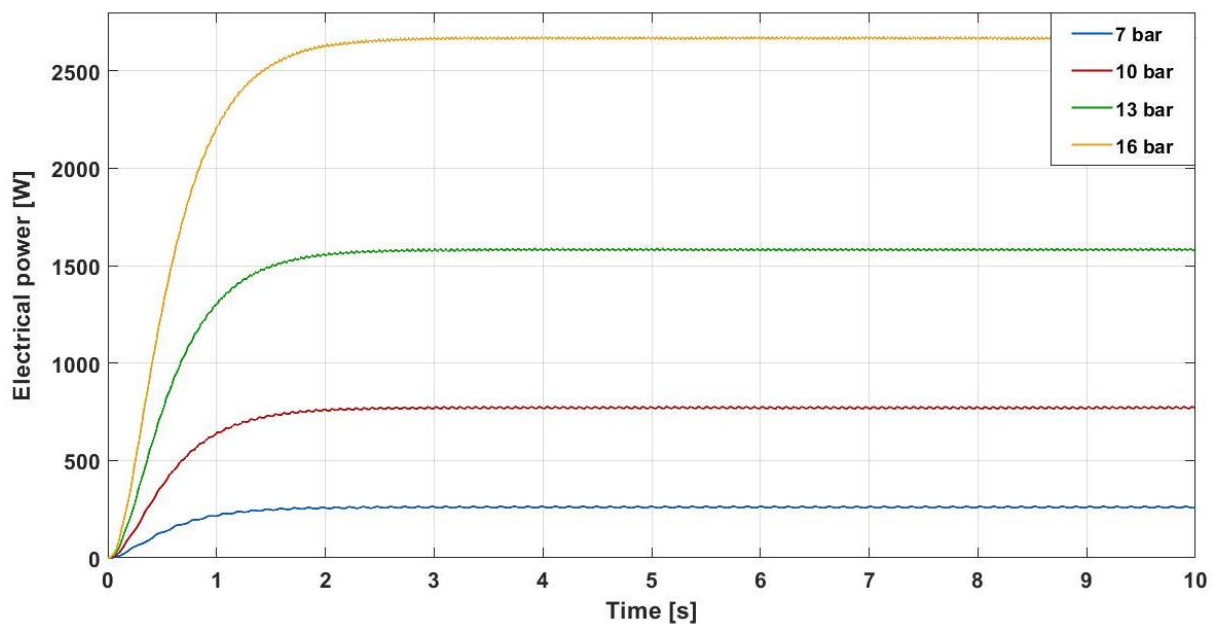


FIGURE 7.3 ELECTRIC POWER WITH DIFFERENT INLET PRESSURES

TABLE 7.1

		Inlet pressure				
		7 [bar]	10 [bar]	13 [bar]	16 [bar]	
η_{is}	Isentropic efficiency	54.7%	61.4%	68.0%	72.6%	a
η_{mec}	Mechanical efficiency	84.0%	83.3%	82.7%	82.0%	b
η_s	Scroll efficiency	66.8%	78.8%	81.2%	81.5%	c
η_{gen}	DC generator efficiency	26.2%	48.6%	62.7%	70.6%	d
η_{ex}	Exergetic efficiency	37.8%	47.3%	52.6%	55.5%	e
$\int_0^T \dot{Q}_1 dt$	[J]	-168	-370	-611	-871	f
$\int_0^T T_{drive} \omega dt$	[kJ]	3.4	10.0	20.7	35.2	g
$\int_0^T \dot{m}_{1,leak} dt$	[g]	37.6	53.4	69.1	84.7	h

TABLE 7.2

		Inlet pressure				
		7 [bar]	10 [bar]	13 [bar]	16 [bar]	
$\frac{\int_0^T \dot{Q}_1 dt}{\int_0^T T_{drive} \omega dt}$	$\left[\frac{J_{th}}{J_{mec}} \right]$	-0.050	-0.037	-0.030	-0.025	a
$\frac{\int_0^T \dot{Q}_2 dt}{\int_0^T T_{drive} \omega dt}$	$\left[\frac{J_{th}}{J_{mec}} \right]$	-0.010	-0.010	-0.011	-0.012	b
$\frac{\int_0^T \dot{Q}_3 dt}{\int_0^T T_{drive} \omega dt}$	$\left[\frac{J_{th}}{J_{mec}} \right]$	-0.031	-0.006	0.002	0.006	c
$\frac{\int_0^T \dot{Q}_4 dt}{\int_0^T T_{drive} \omega dt}$	$\left[\frac{J_{th}}{J_{mec}} \right]$	-0.025	0.005	0.004	$1.16 \cdot 10^{-4}$	d
$\frac{\int_0^T \dot{Q}_{dis} dt}{\int_0^T T_{drive} \omega dt}$	$\left[\frac{J_{th}}{J_{mec}} \right]$	-0.065	0.010	0.024	0.027	e

TABLE 7.3

	Inlet pressure				
	7 [bar]	10 [bar]	13 [bar]	16 [bar]	
$\frac{\int_0^T \dot{m}_{1,leak} dt}{\int_0^T T_{drive} \omega dt} \left[\frac{g}{J_{mec}} \right]$	0.0112	0.0053	0.0033	0.0024	a
$\frac{\int_0^T \dot{m}_{2,leak} dt}{\int_0^T T_{drive} \omega dt} \left[\frac{g}{J_{mec}} \right]$	0.0118	0.0059	0.0038	0.0028	b
$\frac{\int_0^T \dot{m}_{3,leak} dt}{\int_0^T T_{drive} \omega dt} \left[\frac{g}{J_{mec}} \right]$	0.0095	0.0047	0.0030	0.0021	c
$\frac{\int_0^T \dot{m}_{4,leak} dt}{\int_0^T T_{drive} \omega dt} \left[\frac{g}{J_{mec}} \right]$	0.0070	0.0038	0.0026	0.0019	d

7.2 Axial and radial clearance variation

The second sensitivity analysis has been performed on axial and radial clearances. The values simulated are 15, 30, 45, 60 μm . First of all is essential to notice that the pressure in the chambers remains similar in all the cases. In Table 7.4 are collected the integral averages (ratio between the integral of the pressure over time and the simulation duration) of the pressure of all the expansion chambers during the simulation. The fact that the pressures are similar for the four cases implies that even the produced torques do not vary much since they depend on the tangential forces which, in turn, depend on the pressure differences between the chambers. In Figure 7.4 are shown the torques for the four cases between 5 and 5.5 seconds. It is possible to see that the variations are small. Looking at equation 3.25 is clear that if the torques and inertia moments are similar also the angular accelerations are similar and so also the angular speeds. In Figure 7.5 are depicted the angular speeds of the shaft for the four cases. Also in this case is possible to see that there are not sensible variations.

It is useful to imagine the inlet mass flow as if it were made up of two components: the first expands the volume of the chambers and generates useful mechanical power; the second leaks between the chambers. In Table 7.5 this phenomenon is quantified: row a collects the mass of inlet air during the simulation, row b the mass leaked from the first chamber and row c the difference between these two quantities. The latter is practically constant. The same observation applies to the remaining expansion chambers. This means that the mass of air that produces the mechanical energy it is almost the same for the four cases. The rest of the air is necessary to produce the correct pressure difference between the chambers to generate

motion. In Figure 7.7 are depicted the outlet temperature for all the cases. It can be seen that the greater the axial and radial clearances the higher the outlet temperature. This can be explained noting that increasing the clearances also the warmer leaked flow from the previous chambers grows inducing the rise of the chamber temperature.

TABLE 7.4

	Axial and radial gap				
	15 [μm]	30 [μm]	45 [μm]	60 [μm]	
$\frac{\int_0^T P_1 dt}{T}$ [bar]	9.96	9.92	9.87	9.81	a
$\frac{\int_0^T P_2 dt}{T}$ [bar]	7.04	6.87	6.78	6.70	b
$\frac{\int_0^T P_3 dt}{T}$ [bar]	3.59	3.90	4.04	4.10	c
$\frac{\int_0^T P_4 dt}{T}$ [bar]	2.46	2.70	2.81	2.88	d

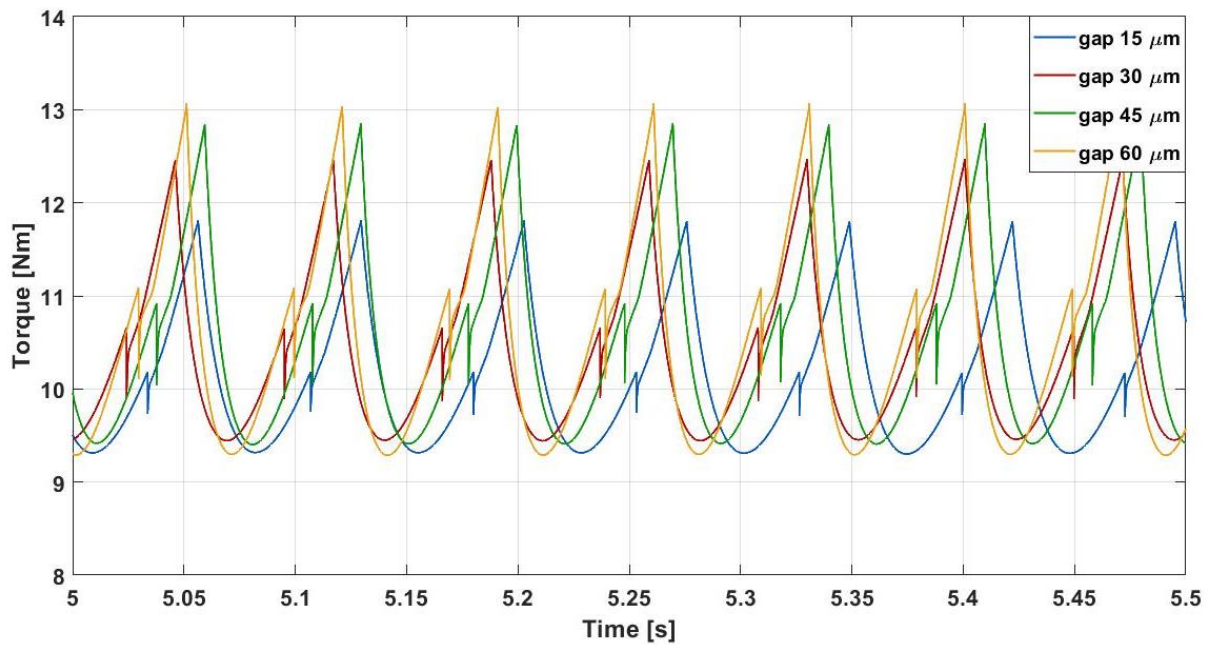


FIGURE 7.4 TORQUE WITH DIFFERENT AXIAL AND RADIAL CLEARANCES

TABLE 7.5

		Axial and radial gap				
		15 [μm]	30 [μm]	45 [μm]	60 [μm]	
$\int_0^T \dot{m}_{1,in} dt$	[g]	121.9	177.0	230.2	281.9	a
$\int_0^T \dot{m}_{1,leak} dt$	[g]	53.4	106.9	160.0	212.2	b
$\int_0^T (\dot{m}_{1,in} - \dot{m}_{1,leak}) dt$	[g]	68.5	70.1	70.2	69.7	c
$\int_0^T \dot{m}_{2,leak} dt$	[g]	59.2	113.0	165.1	216.2	d
$\int_0^T \dot{m}_{3,leak} dt$	[g]	47.4	99.0	151.1	202.7	e
$\int_0^T \dot{m}_{4,leak} dt$	[g]	38.0	90.5	143.1	194.7	f

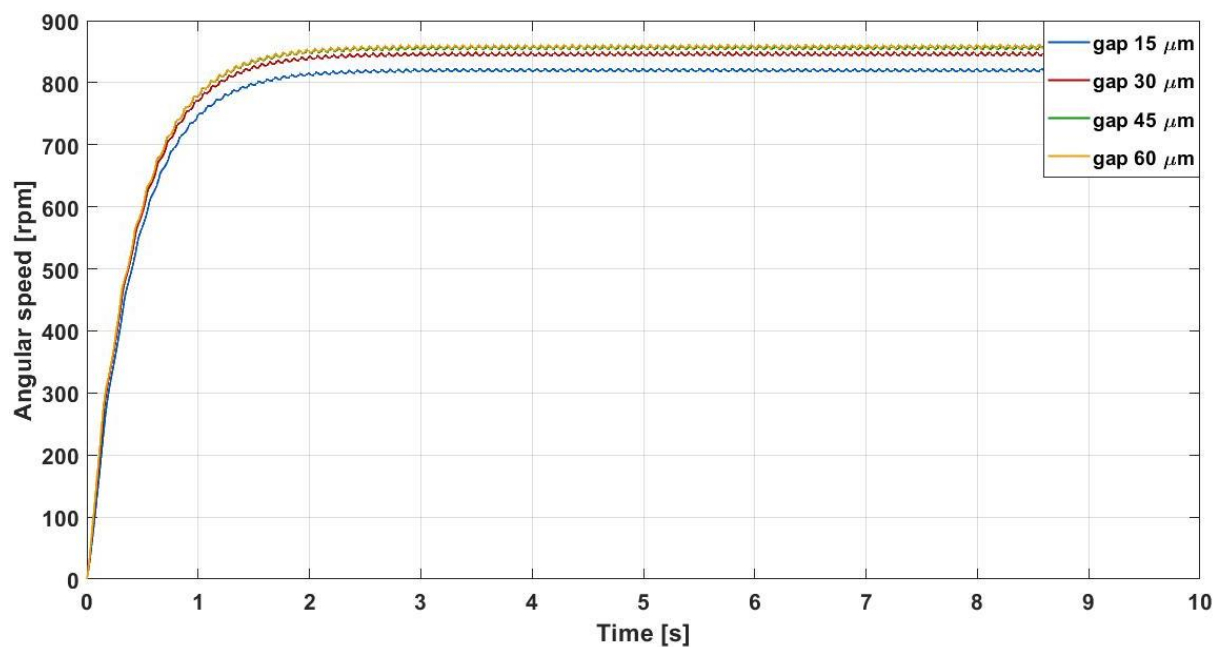


FIGURE 7.5 ANGULAR SPEED WITH DIFFERENT AXIAL AND RADIAL CLEARANCES

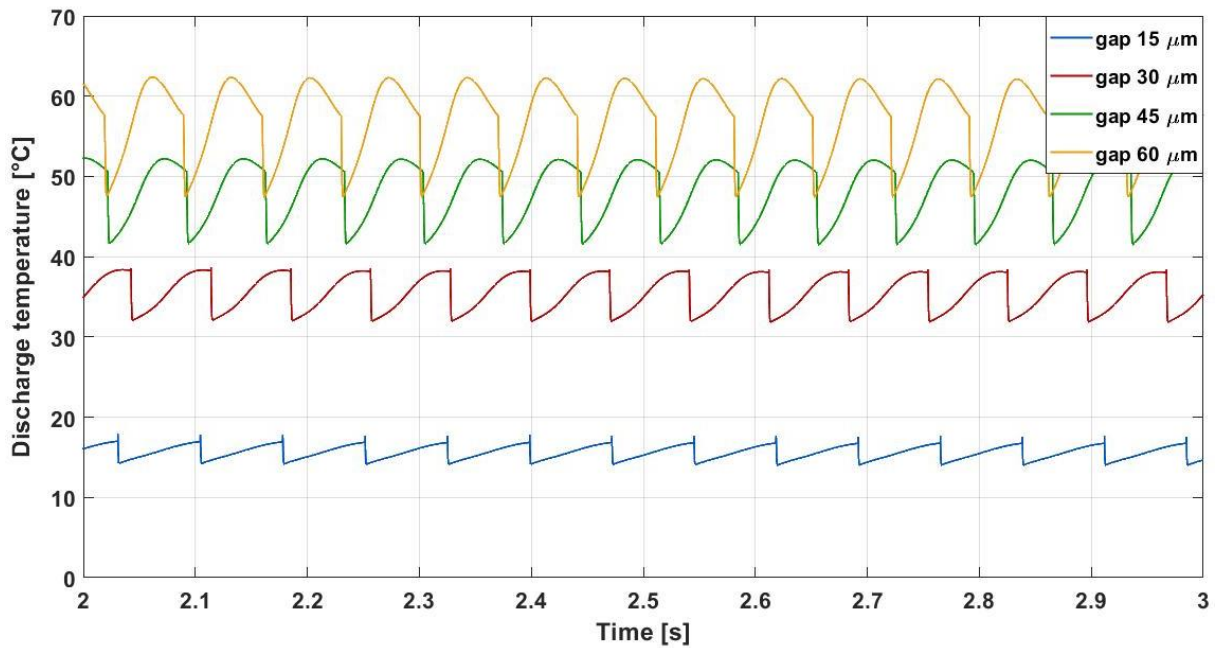


FIGURE 7.7 OUTLET TEMPERATURE WITH DIFFERENT AXIAL AND RADIAL CLEARANCES

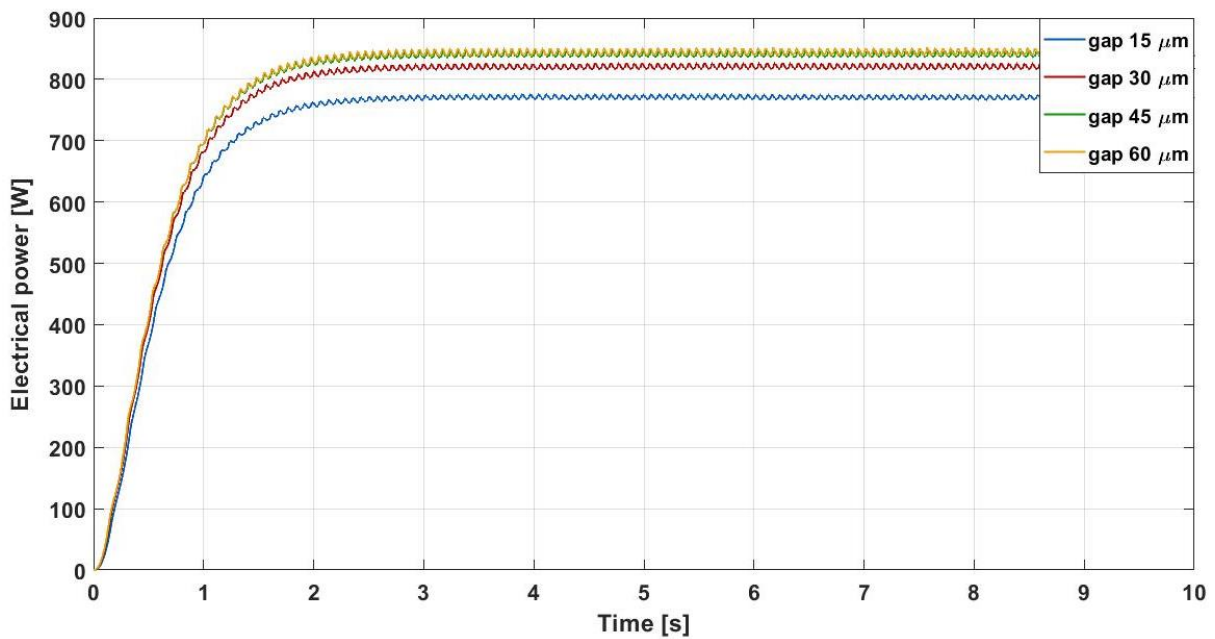


FIGURE 7.6 ELECTRIC POWER WITH DIFFERENT AXIAL AND RADIAL CLEARANCES

In Figure 7.6 is shown the electric power produced in the four cases. Since the torque and the angular velocity are similar for the four cases also their product, the mechanical power, does not change much. Being the electric power strictly correlated to the mechanical one also the latter remains almost the same varying the clearances. In Table 7.6 are listed the efficiencies in

the different cases. The mechanical efficiency does not change because the angular speeds are analogue. As for the mechanical efficiency the DC generator efficiency remains almost constant because the electrical power produced is approximately the same. The isentropic efficiency reduces increasing radial and axial clearances because the mass of leaked air grows with a rate greater than that of the mechanical energy. This is clear looking at row g and h of Table 7.6, to a mechanical energy that remains constant corresponds four times increase of the mass leaked from chamber 1. In Table 7.8 are gathered all the ratios between the leaked mass air and the mechanical energy produced. All of them increase passing from 15 to 60 μm . For the heat exchanged is not possible to carry out the same observation. Looking at the Table 7.7 sometimes the ratio between the heat exchanged and the mechanical energy reduces other times increases and so is not possible to describe a clear trend for the thermal power exchanged. It is important to remember that the term \dot{Q} is the algebraic sum of all the thermal powers and so, if its integral is 0, it does not mean that there have been not thermal exchanges. For the exergetic efficiency can be realize the same reasoning of the isentropic efficiency, the only difference is that the outlet temperature is the simulated one and not that isentropic. The scroll efficiency decreases slightly because the numerator remains approximately constant while the denominator slightly grows.

TABLE 7.6

		Axial and radial gap				
		15 [μm]	30 [μm]	45 [μm]	60 [μm]	
η_{is}	Isentropic efficiency	61.4%	46.9%	37.7%	31.4%	a
η_{mec}	Mechanical efficiency	83.4%	83.3%	83.3%	83.3%	b
η_s	Scroll efficiency	78.8%	76.2%	75.1%	74.1%	c
η_{gen}	DC generator efficiency	48.6%	50.0%	50.5%	50.6%	d
η_{ex}	Exergetic efficiency	47.3%	34.9%	27.6%	22.8%	e
$\int_0^T \dot{Q}_1 dt$ [J]		-370	-293	-229	-183	f
$\int_0^T T_{drive} \omega dt$ [kJ]		10.0	10.7	10.9	11.0	g
$\int_0^T \dot{m}_{1,leak} dt$ [g]		53.4	107.0	160.0	212.2	h

TABLE 7.7

	Axial and radial gap				
	15 [μm]	30 [μm]	45 [μm]	60 [μm]	
$\frac{\int_0^T \dot{Q}_1 dt}{\int_0^T T_{drive} \omega dt} \left[\frac{J_{th}}{J_{mec}} \right]$	-0.0369	-0.0274	-0.0209	-0.0167	a
$\frac{\int_0^T \dot{Q}_2 dt}{\int_0^T T_{drive} \omega dt} \left[\frac{J_{th}}{J_{mec}} \right]$	-0.0095	-0.0021	-0.0019	-0.0035	b
$\frac{\int_0^T \dot{Q}_3 dt}{\int_0^T T_{drive} \omega dt} \left[\frac{J_{th}}{J_{mec}} \right]$	-0.0059	-0.0137	-0.0143	-0.0131	c
$\frac{\int_0^T \dot{Q}_4 dt}{\int_0^T T_{drive} \omega dt} \left[\frac{J_{th}}{J_{mec}} \right]$	0.0046	-0.0094	-0.0153	-0.0194	d
$\frac{\int_0^T \dot{Q}_{dis} dt}{\int_0^T T_{drive} \omega dt} \left[\frac{J_{th}}{J_{mec}} \right]$	0.0096	-0.0106	-0.0251	-0.0358	e

TABLE 7.8

	Axial and radial gap				
	15 [μm]	30 [μm]	45 [μm]	60 [μm]	
$\frac{\int_0^T \dot{m}_{1,leak} dt}{\int_0^T T_{drive} \omega dt} \left[\frac{g}{J_{mec}} \right]$	0.0053	0.0100	0.0146	0.0193	a
$\frac{\int_0^T \dot{m}_{2,leak} dt}{\int_0^T T_{drive} \omega dt} \left[\frac{g}{J_{mec}} \right]$	0.0059	0.0106	0.0151	0.0197	b
$\frac{\int_0^T \dot{m}_{3,leak} dt}{\int_0^T T_{drive} \omega dt} \left[\frac{g}{J_{mec}} \right]$	0.0047	0.0093	0.0138	0.0185	c
$\frac{\int_0^T \dot{m}_{4,leak} dt}{\int_0^T T_{drive} \omega dt} \left[\frac{g}{J_{mec}} \right]$	0.0038	0.0085	0.0131	0.0177	d

Chapter 8

Conclusion

The model presented in this thesis is a valid starting point for the design of scroll expanders in micro-small systems for the recovery of waste heat. Looking at the results of the simulations it is possible to list the following conclusions:

1. Scroll expanders have a high isentropic efficiency although they generate low powers.
2. Any action that increases the angular velocity has a positive effect as it reduces the weight of losses due to heat exchanges and leaks. At the same time, the angular velocity cannot be too high to avoid poor mechanical efficiency.
3. Scroll expanders cannot process high inlet pressures since the end expansion temperature must be higher than that of the environment.
4. The expander efficiency is strongly influenced by radial and axial clearances. Few hundredths of millimeter can produce a drastic increase of leaks causing a reduction of the efficiency.
5. Would be appropriate to use a DC generator with permanent magnets to avoid the supply of electricity to the excitation winding.

All these conclusions agree with the studies that have been already published in the scientific literature. The main advantages of the model presented in this thesis are the short simulation time and the absence of a calibration phase. All this leads to a reduction of the design cost that could have a positive effect on the diffusion of the scroll expander technology.

Nomenclature

<i>a</i>	basic circle radius	[m]	<i>A</i>	area	[m ²]
<i>b</i>	exergy	[J/kg]	<i>A_{max}</i>	oscillating amplitude	[m]
<i>c_p</i>	constant pressure specific heat	[J/kg/K]	<i>c_v</i>	constant volume specific heat	[J/kg/K]
<i>D_c</i>	diameter of scroll curvature	[m]	<i>D_h</i>	hydraulic diameter	[m]
<i>E_a</i>	electromotive force	[V]	<i>f</i>	flow coefficient	-
<i>f_o</i>	oscillating frequency	[s ⁻¹]	<i>f_{sg}</i>	overall dynamic friction coefficient of scroll and generator	[Nm s]
<i>F</i>	force	[N]	<i>h</i>	enthalpy - height	[J/kg] [m]
<i>I_a</i>	current	[A]	<i>J</i>	moment of inertia	[kg m ²]
<i>K_e</i>	constant of electromotive force	[V s rad ⁻¹]	<i>K_t</i>	torque constant	[Nm A ⁻¹]
<i>l</i>	length	[m]	<i>L_a</i>	armature inductance	[H]
<i>m</i>	mass	[kg]	<i>ṁ</i>	mass flowrate	[kg/s]
<i>N_c</i>	expansion chambers number	-	<i>Nu</i>	Nusselt number	-
<i>P</i>	pressure	[Pa]	<i>Pit</i>	scroll pitch	[m]
<i>Pr</i>	Prandtl number	-	<i>Q</i>	heat	[J]
<i>Q̇</i>	heat transfer rate	[W]	<i>R</i>	resistance - radius	[Ω] [m]
<i>Re</i>	Reynolds number	-	<i>St</i>	Strouhal number	-
<i>s</i>	entropy	[J/kg/K]	<i>t</i>	time – thickness	[s] [m]
<i>T</i>	torque - temperature	[Nm] [K]	<i>u</i>	internal energy	[J/kg]
<i>Ū</i>	mean flow velocity	[m/s]	<i>V</i>	volume	[m ³]
<i>Ẇ</i>	rate of work output	[W]	<i>x, y</i>	cartesian coordinate	

Greek letters

α	initial involute angle	[rad]	α_{amb}	ambient heat transfer coefficient	[W/m ² /K]
γ	angle used in scroll modification	[rad]	δ	gap	[m]
η	efficiency	-	λ	thermal conductivity	[W/m/K]
ρ	radius of involute - density	[m] [kg/m ³]	φ	involute angle	[rad]
φ_p	involute angle of tip point	[rad]	ω	angular velocity	[rad/s]

Subscripts

a	axial	amb	ambient
arm	armature	C	Chamber\
C_i	i-th chamber	d	drive
DB	Dittus-Boelter	$down$	downstream
$disc$	disconnection	dis	discharge
e	end	em	electromechanical
ex	exergetic	f	fixed scroll - flank
fr	friction	gen	generator
i	inner	in	inlet
is	isentropic	l	leak\leakage
$load$	electric load	$loss$	loss
mc	circular cutter modification	mec	mechanical
o	outer	orb	orbiting
out	outlet	p	base plate
r	radial	s	scroll

sh shell

t tangent

WF working fluid

sha shaft

up upstream

Bibliography

- [1] BP, "BP Energy Outlook - 2019 edition," 2019.
- [2] C. Hall, J. Lambert and S. Balogh, "EROI of different fuels and the implications for society," Elsevier, 2013.
- [3] M. Astolfi and T. Tartière, "A World Overview of the Organic Rankine Cycle Market," in *IV International Seminar on ORC Power Systems*, Milano, 2017.
- [4] P. Colonna, E. Casati, C. Trapp, T. Mathijssen, J. Larjola, T. Turunen-Saaresti and A. Uusitalo, "Organic Rankine Cycle Power Systems: From the Concept to Current Technology, Applications, and an Outlook to the Future," 2015.
- [5] O. Dumont, A. Parthoens, R. Dickes and V. Lemort, "Experimental investigation and optimal performance assessment of four volumetric expanders (scroll, screw, piston and roots) tested in a small-scale organic Rankine cycle system," Elsevier, 2018.
- [6] T. Yanagisawa, T. Shimizu, M. Fukuta and T. Handa, "Study on Fundamental Performance of Scroll Expander," J-STAGE, 1988.
- [7] Air squared, "Scroll expanders," [Online]. Available: <https://airsquared.com/products/scroll-expanders/e22h038b-l-sh/>.
- [8] M. Zhiwei, B. Huashan and A. P. Roskilly, "Dynamic modelling and experimental validation of scroll expander for small scale power generation system," Elsevier Ltd, 2016.
- [9] S. Quoilin, Sustainable energy conversion through the use of organic rankine cycles for waste heat recovery and solar applications (Ph.D. Thesis), Liege, 2011.
- [10] I. H. Bell, E. A. Groll, J. E. Braun and G. B. King, "Update on compressor scroll chamber geometry," 2010.
- [11] S. Emhardt, G. Tian and J. Chew, "A review of scroll expander geometries and their performance," Elsevier Ltd, 2018.
- [12] J. Wang, X. Luo, L. Yang, L. M. Shpanin, N. Jia, S. Mangan and J. W. Derby, "Mathematical modeling study of scroll air motors and energy efficiency analysis-part II," SAGE, 2011.
- [13] T. D. Eastop and A. McConkey, Applied thermodynamics for engineering technologists, Singapore: Longman, 1993.
- [14] J. Heywood, Internal combustion engine fundamentals, New York: McGraw-Hill, 1988.

- [15] Y. Zhao, L. Li and P. Shu, Thermodynamic simulation of scroll compressor/expander module in automotive fuel cell engine, 2006.
- [16] K. Jang and S. Jeong, "Experimental investigation on convective heat transfer mechanism in a scroll compressor," Elsevier, 2006.
- [17] T. Kenjo and S. Nagamori, Permanent-magnet and brushless DC motors, Oxford: Clarendon Press, 1985.
- [18] R. Krishnan, Permanent magnet synchronous and brushless DC motor drives, CRC Press, 2009.
- [19] I. Bell, "Theoretical and experimental analysis of liquid flooded compression in scroll compressors (Ph.D. Thesis)," Purdue University, 2011.
- [20] J. Hugenroth, J. Braun, E. Groll and G. King, "Liquid-flooded ericsson cycle cooler part 2 - experimental results," Air cond. conf. Purdue Paper, 2006.
- [21] B. Woodland, J. Braun, E. Groll and T. Horton, "Experimental testing of an organic rankine cycle with scroll-type expander," Purdue University, 2012.
- [22] L. C. Mendoza, J. Navarro-Esbri, J. C. Bruno, V. Lemort and A. Coronas, "Characterization and modelling of a scroll expander with air and ammonia as working fluid," Elsevier, 2014.
- [23] L. C. Mendoza, D. Ayou, J. Navarro-Esbri, J. C. Bruno and A. Coronas, "Small capacity absorption systems for cooling and power with a scroll expander and ammonia based working fluid," Elsevier, 2014.
- [24] M. Kane, D. Larrain, D. Favrat and Y. Allani, "Small hybrid solar power system," Elsevier, 2003.
- [25] R. Zanelli and D. Favrat, "Experimental investigation of a hermetic scroll expander-generator," Purdue e-Pubs, 1994.
- [26] H. Wang, R. B. Peterson and T. Herron, "Experimental performance of a compliant scroll expander for an organic rankine cycle," Oregon State University, 2009.
- [27] V. Lemort, S. Declaye and S. Quoilin, "Experimental characterization of a hermetic scroll expander for use in a micro-scale rankine cycle," SAGE journals, 2011.
- [28] Y.-Q. Feng, T.-C. Hung, S.-L. Wu, C.-H. Lin, B.-X. Li, K.-C. Huang and J. Qin, "Operation characteristic of a R123-based organic rankine cycle depending on working fluid mass flow rates and heat source temperature," Elsevier, 2017.
- [29] T. Yanagisawa, M. Fukuta, Y. Ogi and T. Hikichi, "Performance of a oil-free scroll-type air expander," Researchgate, 2001.
- [30] S.-C. Yang, T.-C. Hung, Y.-Q. Feng, C.-J. Wu, K.-W. Wong and K.-C. Huang, "Experimental investigation on a 3 kW organic rankine cycle for low-grade waste heat under different operation parameters," Elsevier, 2017.

- [31] K. Qiu, M. Thomas and M. Douglas, "Investigation of a scroll expander driven by compressed air and its potential applications to orc.," Elsevier, 2018.
- [32] S. Declaye, S. Quoilin, G. Ludovic and V. Lemort, "Experimental study on an open-scroll expander integrated into an ORC (organic rankine cycle) system with R245fa as working fluid," Elsevier, 2013.
- [33] V. Lemort, S. Quoilin, C. Cuevas and J. Lebrun, "Testing and modelling a scroll expander integrated into an organic rankine cycle," Elsevier, 2009.
- [34] R. B. Peterson, H. Wang and T. Herron, "Performance of a small-scale regenerative rankine power cycle employing a scroll expander," SAGE journals, 2008.
- [35] V. Verda and E. Guelpa, "Metodi termodinamici per l'uso efficiente delle Risorse Energetiche," ESCULAPIO, 2015.
- [36] N. Giupponi, "Modelling and simulation of a scroll expander for micro-ORC applications," 2015.
- [37] J. Wang, L. Yang, X. Luo, S. Mangan and J. W. Derby, "Mathematical modelling study of scroll air motors and energy efficiency analysis-Part I," IEEE/ASME TRANSACTIONS ON MECHATRONICS, 2011.
- [38] G. Liu, Z. Yuanyang, Q. Yang, L. Wang, B. Tang and L. Li, "Theoretical and experimental research on scroll expander used in small-scale organic Rankine System," 2013.
- [39] G. Liu, Y. Zhao, L. Li and P. Shu, "Simulation and experimental research on wide ranging working process of scroll expander driven by compressed air," 2010.
- [40] Y. Chen, N. P. Halm, E. A. Groll and J. E. Braun, "Mathematical modeling of scroll compressors - Part I: Compression process modeling," International Journal of Refrigeration, 2002.
- [41] Y. Liu, C. Hung and Y. Chang, "Design optimization of scroll compressor applied for frictional," Elsevier, 2009.
- [42] Nidec, "LSK - D.C. motors 2 to 750 kW," [Online]. Available: https://www.leroy-somer.com/documentation_pdf/3805_en.pdf.
- [43] M. White and A. I. Sayma, "The impact of component performance on the overall cycle performance of small-scale low temperature organic Rankine," in *Materials Science and Engineering 90 (2015) 012063*, 2015.
- [44] R. Wang, G. Kuang, L. Zhu, S. Wang and J. Zhao, "Experimental Investigation of a 300 kW Organic Rankine Cycle Unit with Radial Turbine for Low-Grade Waste Heat Recovery," 2019.
- [45] R. Pili, N. Siamisiis, R. Agromayor, L. O. Nord, C. Wieland and H. Spliethoff, "Efficiency correlations for off-design performance prediction of orc axial-flow turbines," in *5th International Seminar on ORC Power Systems*, Athens, 2019.

- [46] L. Pan and H. Wang, "Experimental Investigation on Performance of an Organic Rankine Cycle System Integrated with a Radial Flow Turbine," 2019.
- [47] B. Peng, B. Zhu and V. Lemort, "Theoretical and experimental analysis of scroll expander," Purdue e-Pubs, 2016.